

\_\_\_\_\_  
Unterschrift BetreuerIn



TECHNISCHE  
UNIVERSITÄT  
WIEN  
Vienna University of Technology

## DIPLOMARBEIT

# Investigation of a MEMS Electric Field Sensor based on Alternating Charges

ausgeführt am Institut für Sensor- und Aktuatorssysteme  
der Technischen Universität Wien

unter der Anleitung von  
**Ao.Univ.Prof.Dipl.-Ing.Dr.techn. Franz Keplinger**  
**Dipl.-Ing.Dr.techn. Andreas Kainz**

durch

**Markus Demel, BSc.**

Gusshausstrasse 27-29 / E366  
1040 Wien

March 24, 2020

\_\_\_\_\_  
Unterschrift StudentIn



Die approbierte gedruckte Originalversion dieser Diplomarbeit ist an der TU Wien Bibliothek verfügbar.  
The approved original version of this thesis is available in print at TU Wien Bibliothek.



Die approbierte gedruckte Originalversion dieser Diplomarbeit ist an der TU Wien Bibliothek verfügbar.  
The approved original version of this thesis is available in print at TU Wien Bibliothek.

# Abstract

This thesis is centered around measuring and quantifying static electric fields. There is an abundance of approaches for such a sensor but none of them is satisfying with respect to practicability, reliability and reproducibility. Through the usage of microsystem technology it is possible to build sensors with spatial resolutions in the region of milli- to micrometers. Therefore, meeting scientific and industrial demands which have been out of reach until now. Furthermore, these sensors are capable of measuring low-frequency and static electric fields with minimal external interference.

In order to provide such a sensor, a method was developed to design such devices with a variety of geometries. Those devices have been manufactured in silicon and prepared for further characterization.

An appropriate setup has been built and used to measure the properties of several different types of sensor structures. The data of these measurements has been evaluated and the characteristics of the sensors were compared during this thesis. This lead and will lead to more insight into the behavior of this kind of sensor.

# Kurzfassung

Diese Arbeit befasst sich im weitesten Sinne mit der Erfassung der Eigenschaften elektrischer Felder. Obwohl es bereits einige vielversprechende Ansätze gibt, erfüllt dennoch keiner alle Kriterien vieler Einsatzgebiete. Durch die Entwicklung eines Sensors auf MEMS-Basis soll es möglich werden, elektrische Feldsensoren mit örtlichen Auflösungen im Millimeter- oder sogar Mikrometerbereich herzustellen und damit wissenschaftliche aber auch industrielle Anforderungen an diese Messungen zu erfüllen. Weiters sollen die, in dieser Arbeit behandelten, Sensoren auch die Möglichkeit bieten niederfrequente elektrische Felder ohne zwischenzeitliche Eingriffe, wie zum Beispiel Kalibrierungen, zu messen.

Zu diesem Zweck wurde eine Methode entwickelt, mehrere verschiedene Strukturen mit unterschiedlichsten geometrischen Parametern herzustellen. Mit Hilfe eines Silizium-Wafers und den geeigneten Ätzverfahren wurden die erstellten Strukturen verarbeitet und zur Anwendung vorbereitet.

Ein geeigneter Aufbau zur Vermessung eines erzeugten elektrischen Feldes wurde erstellt und die Strukturen in weiterer Folge einzeln vermessen und charakterisiert. Diese Messdaten konnten in dieser Arbeit zum Teil ausgewertet werden und die Eigenschaften unterschiedlicher geometrischer Formen miteinander verglichen werden.

Dies führte zu einigen Erkenntnissen welche sich für die weitere Entwicklung als hoffentlich wertvoll und wegweisend herausstellen werden.



Die approbierte gedruckte Originalversion dieser Diplomarbeit ist an der TU Wien Bibliothek verfügbar.  
The approved original version of this thesis is available in print at TU Wien Bibliothek.

# Contents

<b>1. Introduction</b>	<b>1</b>
<b>2. Sensor</b>	<b>2</b>
2.1. Fundamentals . . . . .	2
2.1.1. Electrostatic Fundamentals . . . . .	2
2.1.2. Mechanical Fundamentals . . . . .	5
2.2. Sensor principle . . . . .	10
2.2.1. Sensor responsivity . . . . .	11
2.2.2. Sensor setup . . . . .	12
2.3. Fields of application . . . . .	13
2.3.1. Atmospheric measurement . . . . .	13
2.3.2. Health effects . . . . .	14
2.4. State of the art . . . . .	15
2.4.1. Electric field mill . . . . .	15
2.4.2. Induction probes . . . . .	19
2.4.3. Optical sensors . . . . .	20
<b>3. Sensor Design</b>	<b>21</b>
3.1. Mask Design . . . . .	21
3.2. Simulation . . . . .	23
3.3. Manufacturing . . . . .	25
<b>4. Measurements</b>	<b>27</b>
4.1. Measurement setup . . . . .	27
4.1.1. Field generation . . . . .	27
4.1.2. Sensor Control . . . . .	29
4.1.3. Sensor . . . . .	30
4.1.4. Readout . . . . .	31
4.2. Measurements . . . . .	35
<b>5. Results</b>	<b>39</b>
5.1. I-Cantilevers . . . . .	39
5.2. T-Cantilever . . . . .	44
5.3. U-Cantilever . . . . .	46

5.4. PCB Carrier . . . . .	48
<b>6. Conclusion and Outlook</b>	<b>49</b>
6.1. Conclusion . . . . .	49
6.2. Outlook . . . . .	50
<b>A. Appendix</b>	<b>i</b>
A.1. Measurement results . . . . .	i
A.1.1. I-cantilever . . . . .	i
A.1.2. T-cantilever . . . . .	ii
A.1.3. U-cantilever . . . . .	iii
<b>Bibliography</b>	<b>iv</b>



# 1. Introduction

The electric field describes the force a test-charge is subjected to while near another charge. The knowledge of its strength and direction can be of utmost value for many different applications such as lightning research, high-voltage power line safeguarding and laboratory applications. A reliable way of measuring such electric fields in a simple and compact way, while maintaining a decent resolution and reliability has not been reported yet.

One promising approach with high spatial resolution is based on micro electro mechanical system technology. MEMS technology is able to produce sensors and actuators with dimensions in the micrometer range. These devices are more efficient and cheaper than their macroscopic counterparts. By utilizing such a MEMS device, a structure with dimensions in the milli- to micrometer range can be manufactured on which an electrical charge is applied. When exposed to an electric field a force will be exerted on the structure influencing its motion. This deflection is measured and allows to deduce the strength as well as the direction of the electric field.

This thesis is centered around that approach. Its main focus lies on the manufacturing and characterisation of different structures exploring their properties, advantages and disadvantages. The design of those structures revolves around their bending behavior. Therefore it is interesting to investigate the different behavior when varying the shape, length, width and even adding substructures. Every change leads to a different eigenfrequency and capacitance of the sensor, subsequently changing its response force in a given external electric field and therefore, changing its responsivity. A significant number of those structures were manufactured and characterised. The measurement process was performed by utilising a laser-Doppler vibrometer, looking at the change of deflection while the sensor is placed in an electric field. These measurements are to be discussed in this thesis.

## 2. Sensor

The importance of measuring electric fields is made evident by the abundance of approaches of respective sensors. Over the last few decades many groups from different fields have developed numerous measurement principles, each of them with their own advantages and disadvantages.

The measuring principle applied within the presented cantilever-based sensor is based on neither of these, but utilizes an elementary concept of physics, while being able to neglect some of the negative effects of other approaches. To fully understand the principle of operation of the sensor the fundamentals of the electric and the magnetic field as well as the mechanics of a beam structure shall be covered in the following sections.

### 2.1. Fundamentals

To describe the principle of the sensor treated in this thesis two major physical processes are involved. Section 2.1.1 covers the electrostatic fundamentals of the sensor transduction, while section 2.1.2 addresses the mechanical aspect.

#### 2.1.1. Electrostatic Fundamentals

##### Electric field

The electric field describes the force a charged particle would be exposed to in the vicinity of another charge [1, 2]. It is the vector field of the electric field strength. When a charged element is put between two differently charged elements, it experiences a force depending on the charges and their distance. This setup is best described by a common plate capacitor.

The potential inside a capacitor at coordinate  $x$  is described by

$$\phi(x) = -\frac{U}{d}x + \phi_1, \quad (2.1)$$

with  $U$  being the applied voltage,  $d$  the distance between the two plates,  $\phi_1$  the potential at one of the plates and  $\phi_2$  the potential at the other.

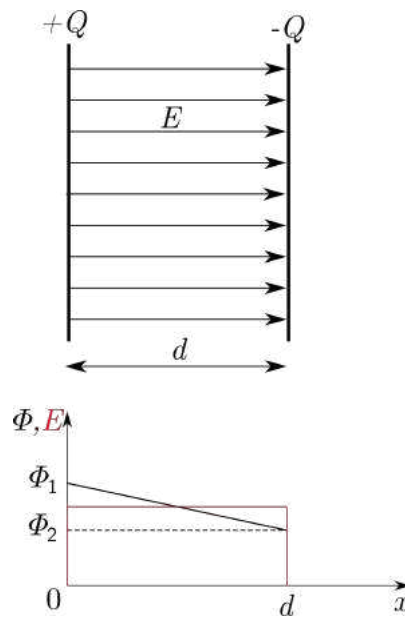


Figure 2.1.: Principle of a plate capacitor.

From this relationship, the electric field can be derived via

$$\mathbf{E} = -\text{grad}(\phi) = \frac{U}{d} \mathbf{e}_x, \quad (2.2)$$

with  $\mathbf{e}_x$  denoting the unit vector in  $x$ -direction.

## Coulomb force

Coulomb's law is the mathematical description of the interaction of two charged particles [3]. Similar to the gravitational pull one object exerts on another, the electrostatic force a charged particle ( $q_0$ ) exerts on another ( $q_1$ ) can be described by

$$\mathbf{F} = \frac{1}{4\pi\epsilon_0} \frac{q_1 q_0}{(\mathbf{r}_1 - \mathbf{r}_0)^2} \mathbf{e}_r, \quad (2.3)$$

with  $\epsilon_0$  as the vacuum permittivity,  $\mathbf{r}_i$  the positional vector of the respective particle and  $\mathbf{e}_r$  the unit vector from one charge to the other.

From this equation a vector field can be derived by normalizing it as  $\mathbf{F}/q_0$ . The result is the electric field strength of the charge  $q_1$  and its respective vector field, the electric field.

$$\mathbf{E} = \frac{\mathbf{F}}{q_0} = \frac{1}{4\pi\epsilon_0} \frac{q_1}{(\mathbf{r}_1 - \mathbf{r}_0)^2} \mathbf{e}_r. \quad (2.4)$$

The unit of the electric field is written as:

$$[\mathbf{E}] = \left[ \frac{F}{q} \right] = \frac{\text{N}}{\text{A} \cdot \text{s}} = \frac{\text{V}}{\text{m}} \quad (2.5)$$

As can be seen in Eq. (2.4), the electric field of a particle and the exerted force on another particle are directly linked. Therefore it is sufficient to measure one of them to know the other. Although the sensor discussed in this thesis is mainly an electric field sensor, it can be converted into a magnetic field sensor by just a few adjustments.

## Magnetic field

Between two magnetized bodies and/or a moving electric charge, a force can be measured [4]. Similar to the electric field, this force can be described by a force field called the magnetic field. This field is being generated by magnetized materials and additionally by conducting elements with moving charges.

The magnetic field is described by two physical quantities, the magnetic field strength  $\mathbf{H}$  and the magnetic flux density  $\mathbf{B}$ , which, in vacuum, relate to each other as follows

$$\mathbf{B} = \mu_0 \mathbf{H}. \quad (2.6)$$

### Lorentz force

The force addressed in the previous paragraph is called Lorentz force named after Hendrik Antoon Lorentz who dedicated his work to describing the motion of electrons [5]. The force a magnetic field exerts on a moving charge can be described by

$$\mathbf{F} = q\mathbf{v} \times \mathbf{B}. \quad (2.7)$$

This force can be measured by sending a current i.e. moving charges through, e.g. U-shaped sensor structures in an external magnetic field. This causes a deflection which can be determined rather easily.

## 2.1.2. Mechanical Fundamentals

One of the main influences on the dynamics of the sensor is the mechanical movement. It can be conveniently described by a conventional, well understood model. The sensor can be treated as an ordinary beam under the influence of a uniform force load. This model can be further improved upon by applying the quality factor (Sec. 2.1.2), taking the damping of the cantilever into consideration.

### Beam mechanics

The force  $\mathbf{F}$  exerted by the electric field and applied to the charged beam can be approximated as a uniform force load  $q = F/l$  acting on a cantilever beam (Fig. 2.2) [6].

The resulting bending moment of such a beam with length  $L$  and load  $q$  is calculated by

$$M(x) = -\frac{q(L^2 - 2Lx + x^2)}{2}. \quad (2.8)$$

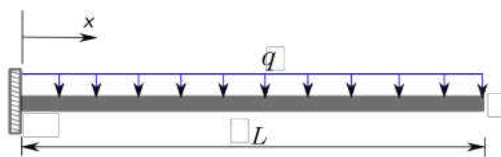


Figure 2.2.: Schematic drawing of a cantilever with an uniform load.

The relation between the bending moment  $M$  and the deflection  $w$  can be written as

$$M(x) = -E_y I_y \frac{d^2 w(x)}{dx^2} \quad (2.9)$$

with  $E_y$  as the Young's modulus and  $I_y$  as the second moment of inertia which for a beam with rectangular cross-section reads  $I_y = \frac{bh^3}{12}$ . This leads to a deflection of

$$w(x) = \frac{q x^2 (6 L^2 - 4 L x + x^2)}{24 E_y I} \quad (2.10)$$

This equation yields the result of a stationary beam under the influence of a uniform load. The problem becomes considerably more difficult when the load is time-dependent.

To solve this sort of beam-bending problem Leonard Euler and Daniel Bernoulli developed a method known as the Euler-Bernoulli beam theory [7, 8]. Neglecting the rotational inertia as well as the shear deformation under the condition of a length-to-height ratio greater than 10, the motion of the beam can be written as

$$\rho A \frac{\partial^2 u(x, t)}{\partial t^2} + E_y I_y \frac{\partial^4 u(x, t)}{\partial x^4} = 0, \quad (2.11)$$

with  $A$  being the area of the cross-section,  $u$  the deflection and  $\rho$  the density of the beam.

To solve this differential equation, a separation-of-variables ansatz is used

$$u(x, t) = \sum_{n=1}^{\infty} U_n(x) \cos(\omega t), \quad (2.12)$$

with  $\omega$  denoting the frequency of the motion and  $n$  the modal number. Furthermore,  $U_n$  can be written as

$$U_n(x) = \underbrace{a_n \cos(\beta_n x) + b_n \sin(\beta_n x)}_{\text{beam movement}} + \underbrace{c_n \cosh(\beta_n x) + d_n \sinh(\beta_n x)}_{\text{clamping influence}}, \quad (2.13)$$

with  $\beta_n$  as the wavenumber and  $a_n, b_n, c_n$  and  $d_n$  denoting free variables minimizing the total energy in the structure. The first two terms represent the movement of a beam neglecting the clamping, while the last two terms take the clamping into account. Combining the equations (2.11), (2.12) and (2.13), the differential equation becomes

$$-\rho A \omega^2 u(x, t) + E_y I_y \beta_n^4 u(x, t) = 0. \quad (2.14)$$

Resulting from this relationship, the eigenfrequency of the beam can be derived, which reads

$$\omega = \beta_n^2 \sqrt{\frac{E_y I_y}{\rho A}}. \quad (2.15)$$

To apply the aforementioned equations to the sensor at hand, the boundary conditions of a clamped beam have to be considered. At the point of clamping the cantilever is fixed in its position resulting in

$$U_n(0) = 0 \quad \text{and} \quad \left. \frac{\partial U_n}{\partial x} \right|_{x=0} = U_n'(0) = 0, \quad (2.16)$$

while the beam experiences no bending or a momentum at its full length yielding

$$\left. \frac{\partial^2 U_n}{\partial x^2} \right|_{x=L} = U_n''(L) = 0 \quad \text{and} \quad \left. \frac{\partial^3 U_n}{\partial x^3} \right|_{x=L} = U_n'''(L) = 0 \quad (2.17)$$

These conditions lead to an expression for the eigenfrequency of

$$\omega_n = \frac{\lambda_n^2}{L^2} \sqrt{\frac{E_y I_y}{\rho A}}, \quad (2.18)$$

with  $\lambda_n = \beta_n L = (2n - 1) \frac{\pi}{2}$ , and numerical values of  $\lambda_{1,2,3} = 1.8751, 4.6941, 7.8548$  for the first three eigenmodes  $n = 1, 2, 3$ . The final result of the calculations beforehand yields the eigenmodes of an oscillating cantilever, Fig.2.3,

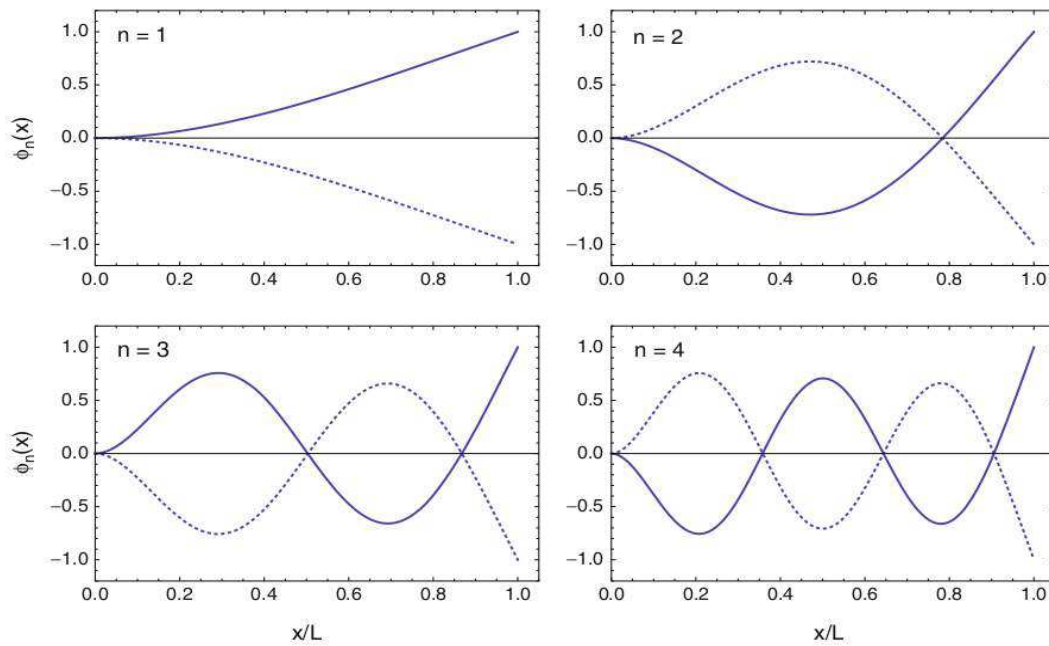


Figure 2.3.: First four eigenmodes of a clamped beam (cantilever).

as well as a normalized function for  $U_n$

$$U_n(x) = U_{0,n} \chi_n(x), \quad (2.19)$$



with

$$\chi_n(x) = \frac{1}{2} [\cos(\beta_n x) - \cosh(\beta_n x) - \frac{\cos(\beta_n L) + \cosh(\beta_n L)}{\sin(\beta_n L) + \sinh(\beta_n L)} (\sin(\beta_n x) - \sinh(\beta_n x))]. \quad (2.20)$$

These calculated frequencies represent the ones at which the sensor will yield the highest output signal and should therefore be driven at.

### Quality factor

To improve the approximation of the mechanical model one has to take the damping of the system into consideration [9]. It is described by the quality factor  $Q$  of the system taking the energy loss through damping during the oscillation into account [10]. The damping is mainly caused by friction inside the material itself. The factor is defined as the ratio of stored energy during one oscillation ( $W$ ) to the lost energy during this period ( $V$ )

$$Q = 2\pi \frac{W}{V}. \quad (2.21)$$

The quality factor of a mechanical oscillating system can be calculated with the differential equation of an ordinary damped ( $d$ ) mass ( $m$ ) - spring ( $k$ ) system in mind

$$m \frac{d^2x}{dt^2} + d \frac{dx}{dt} + kx = 0 \quad \text{or} \quad \frac{d^2x}{dt^2} + 2D\omega_0 \frac{dx}{dt} + \omega_0^2 x = 0, \quad (2.22)$$

with  $\omega_0 = k/m$  being the resonance frequency and  $D = d/(2k)$  the damping ratio. When calculating the energy of the oscillator via its amplitude and using Eq. 2.21, the resulting factor can then be written as

$$Q = \omega_d \frac{m}{d} \approx \frac{\sqrt{m * k}}{d} = \frac{1}{2D}, \quad (2.23)$$

with  $\omega_d$  as the angular eigenfrequency of the damped system and the approximation of  $\omega_d \approx \omega_0$ , which is true for  $D \ll 1$ . Applying this factor to the theoretical mechanical approach yields an approximation for the expected deflection of the cantilever when operated at the resonance frequency.

## 2.2. Sensor principle

The sensor discussed in this thesis relies on the interaction of a charge with a surrounding electric field. This interaction occurs in the form of a mechanical force resulting in a deflection of a compliant structure.

A cantilever, fabricated from single crystal silicone, is charged by applying an

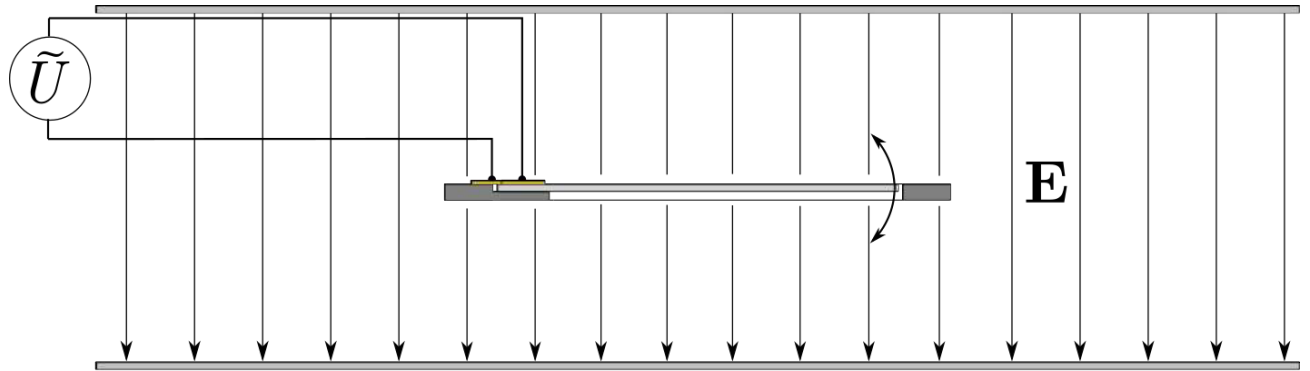


Figure 2.4.: Principle of the discussed sensor.

AC voltage. Therefore, the cantilever has an oscillating potential while the surrounding silicon acts as ground. As described in Sec. 2.1.1, the sensor experiences a force deflecting the cantilever proportional to the strength of the electric field. Furthermore, the frequency of the cantilever voltage is known, making the use of a lock-in amplifier possible and therefore improving the signal-to-noise ratio considerably.

Another aspect to consider is the mechanical stiffness of the beam. In Sec. 2.1.2 the mechanical movement of the cantilever is examined, describing the maximum deflection of a bending beam under the influence of a uniform load as well as a look into the oscillating movement and its influence on the resonance frequency at which the sensor should be driven to achieve the maximum response.

### Cantilever force

The aspects mentioned beforehand lead to an estimation of the cantilever force as follows.

To describe the force the external field exerts on the cantilever, the charges on it have to be known. Those can be calculated by

$$Q(t) = CU(t) \quad (2.24)$$

with  $Q(t)$  as the charge,  $C$  as the capacity of the arrangement and  $U(t)$  as the voltage applied to the sensor. The voltage  $U(t)$  between the cantilever and the surrounding ground is described as

$$U(t) = U_0 \sin(\omega t), \quad (2.25)$$

with  $U_0$  being the amplitude. The potential of the cantilever oscillates around the potential of the surroundings, which is in this case ground. Furthermore, the uniform external electric field  $E$  supplied by parallel field plates is described as

$$E = \frac{U_e}{d}, \quad (2.26)$$

with  $d$  as the distance between the plates. The force  $F$  can now be written as

$$F = QE = CUE = CU_0 \sin(\omega t)E. \quad (2.27)$$

With this force the responsivity of the sensor can be estimated.

### 2.2.1. Sensor responsivity

The force  $F$  can be used to calculate the responsivity of the cantilever which describes the input-output gain of a detector system.

Recalling the deflection of the cantilever from Eq. (2.10),

$$w(x) = \frac{q}{24 E_y I_y} (6 L^2 x^2 - 4 L x^3 + x^4), \quad (2.28)$$

with  $q$  denoting the uniform load and  $x$  the longitudinal coordinate, the maximum deflection at the tip of the beam results in

$$w(L) = \frac{q L^4}{8 E_y I_y}. \quad (2.29)$$

The electrostatic force can be written as a force per length as

$$q = \frac{F}{l}, \quad (2.30)$$

which allows to define an effective stiffness of the cantilever of

$$k = \frac{F}{w(L)} = \frac{8 E_y I_y}{L^3}, \quad (2.31)$$

leading to a mathematical equation involving the external electric field as well as the deflection of the sensor and therefore enabling the calculation of the overall responsivity. The responsivity itself is defined as the ratio of the deflection to the electric field causing it

$$R = \frac{w}{E} = \frac{C U l^3}{8 E_y I_y}. \quad (2.32)$$

With the sensor at hand the responsivity is one of the main characteristics. A higher value leads to a bigger change in signal at the same change in electric field.

### 2.2.2. Sensor setup

The sensor is composed of 3 distinguishable components. The first element excites the sensor at the given eigenfrequency. The second one consists of the electromechanical transducer itself. The third component converts the sensor movement into useable data.

#### Sensor control

Applying the sensor for actual field measurements requires a mobile version of a frequency generator. Therefore the signal has to be generated with a device providing only the most necessary features. In [11] one such device and its development is described. With a combination of capacitors and resistors in conjunction with a

timer IC it is possible to get a frequency and amplitude stable signal driving the cantilever. Furthermore this specific IC requires a driving voltage of only 1.5 V making the usage of a common battery viable and ensuring the portability of the device.

## Readout

The readout of the sensor converts the mechanical movement of the cantilever into useable data. This can be achieved in many ways. The main approach used during the testing of the cantilevers in this thesis is based on the Doppler-effect and subsequently called a laser-Doppler vibrometer. Its attributes make it a fast and reliable method for testing inside the lab, but its bulky setup prevents this readout from being used in field testing. A more in-depth description will be given in Sec. 4.1.

The second approach [12], developed by Martin Gschirtz BSc, may be applied during future field measurements.

It is based on a Michelson interferometer and extends it with a stabilization mechanism to ensure that the signal will always be measured at the optimal working point.

## 2.3. Fields of application

The sensors manufactured in the course of this thesis are aiming to be more accurate, smaller and cheaper to produce than all of the common electric field sensor approaches. This may enable research in fields where the measurement of electric fields is necessary but was restricted by the limitations of state-of-the-art measurement approaches. Some of those fields shall be introduced.

### 2.3.1. Atmospheric measurement

To achieve more insight into atmospheric processes it is necessary to measure the involved phenomena directly. A large number of them is not reproducible in a laboratory. The described method is designed to provide an easy-to-handle, reliable and accurate way to satisfy the needs of atmospheric research.

In the following a few examples of topics in the field of atmospheric research are provided.

**Electric fields in thunderclouds** A thundercloud is subject to three distinct effects [13]. The electric field of the cloud may induce ionization effects above the cloud in the upper atmosphere. Furthermore clouds exert an electric field on the earth itself making their effects senseable and detectable even at ground level. The last effect concerns ionizing radiation. A particle loses energy while traveling, when this particle is subjected to an electric field, it is possible that the deceleration is partly compensated or even reversed leading to an acceleration. Being able to measure the electric field in a thundercloud leads to a better and more in-depth understanding of those effects.

**Upward lightning from tall structures** The magnitude of electric fields built up inside clouds leads to the positive charge at the bottom trying to equalize with structures on the ground [14]. This equalization process manifests itself in the form of lightning, with cloud-ground lightning being the least common but most influential form. To investigate this phenomenon it is of utmost importance to detect the electric field as accurate as possible. Since the most probable location of lightning impact is at the top of tall structures with a point-like field enhancement, a sensor like the one treaded in this thesis enables measurements with a very high spatial resolution, making them easier to apply and handle.

### 2.3.2. Health effects

The interactions of electric fields with the human body are twofold. For one, human body tissue absorbs energy from electric fields [15]. This effect becomes significant at frequencies above 100 kHz, which is not within the range discussed in this thesis. The more significant effect is the coupling of the tissue to an electric field. In the presence of such a field, electric currents are induced inside the body. Furthermore, electric dipoles are formed and their orientation manipulated. This can lead to a diverse range of health effects, ranging from insignificant reactions to cancer inducing reactions up to damage on a cellular scale. For these reasons

it is of utmost importance to limit the exposure of humans to large electric fields (live-line working) and to measure those fields accordingly.

## 2.4. State of the art

State-of-the-art electric field measurement can be divided into 3 main principles, each having their respective application. Those are field mills, induction probes and optical measurement. The following sections are an overview of those.

### 2.4.1. Electric field mill

#### Basic electric field mill approaches

Field mills are based on the measurement of capacitively induced charges or currents on conducting electrodes. There are three main approaches found in literature.

The first and most known approach employs a rotating shutter periodically exposing the conducting electrode to and shielding it from the external field [Fig. 2.5]. During exposing, a charge is induced which leads to a current between the electrode and the ground [16, 17].

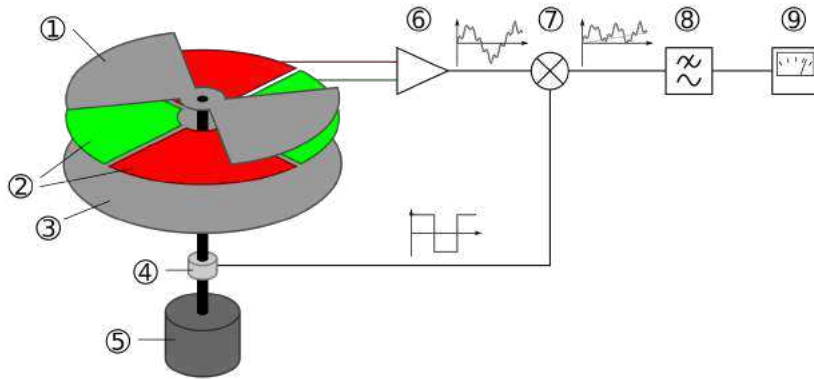


Figure 2.5.: Principle of an electric field mill.

- ① Rotating shutter. ② Segmented electrodes. ③ Base plate. ④ Rotary encoder. ⑤ Drive. ⑥ Amplifier. ⑦ Multiplier. ⑧ Low-pass filter. ⑨ Display.

The electric field can then be derived via:

$$i(t) = \varepsilon_0 E \frac{dA(t)}{dt}, \quad (2.33)$$

where  $i(t)$  denotes the electric current over the time,  $E$  the electric field,  $A(t)$  the exposed area over the time and  $\varepsilon_0$  the dielectric constant. Another approach is the cylindrical field mill. Pioneered by H.W. Kasemir [18] around 1950, it was used to measure the electric field around an aeroplane in all three field-components, especially in high altitudes and in and around thunderclouds.

The cylindrical field mill consists of two cylinder halves working as electrodes [Fig. 2.6].

They are rotating with an angular velocity of  $\omega$  which leads to varying induced charges on the halfcylinders [17]. The induced charge on one of the electrodes can be derived from:

$$q(t) = 4\varepsilon_0 r l E \sin(\omega t), \quad (2.34)$$

with  $q$  being the charge and  $r$  and  $l$  the radius and length of the cylinder respectively. The measured current  $i(t) = q'(t)$  can be written as:

$$i(t) = 4\varepsilon_0 r l E \omega \cos(\omega t), \quad (2.35)$$



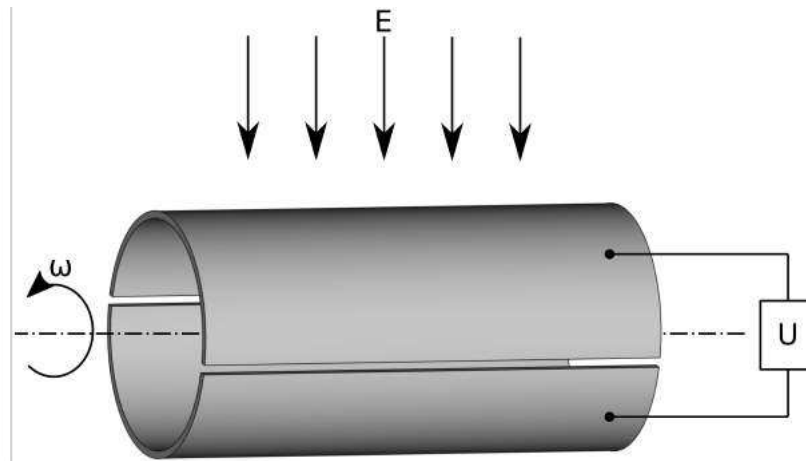


Figure 2.6.: Principle of a rotating cylindrical electric field mill.

The final approach is based upon a vibrating plate [17]. The sensor comprises a plate with an opening serving as one of the electrodes of a capacitor. Beneath that opening a second plate acts as the second electrode of the capacitor. The second electrode is driven by an actuator creating a time-varying voltage between the two, allowing to conclude the properties of the electrical field.

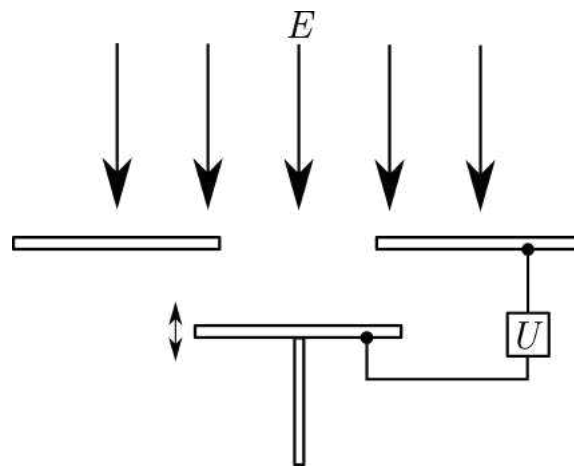


Figure 2.7.: Principle of a vibrating electric field mill

Overall, the field-mill principle enables the measurement of an electric field without any external moving charges during the measurement. It is a well-known and often used measurement technology. The main disadvantages are the conducting parts inside the electric field leading to a severe field distortion and the mechanical wear. The field mill principle is improved upon by using MEMS technology enabling better resolutions while being much smaller.

### MEMS electric field mill

One particular – and for this thesis relevant – approach to the field mill principle is the micro-electro-mechanical one. Where usual electric field mills are designed on a length scale of centimeters or even larger, this approach is operating at the scale of micrometers. To build such devices, special methods and materials have to be used of which are based on silicon.

The basic working principle of the sensor stays the same as on the macroscopical level but the field resolution limits are improved when using the micromachined approach.

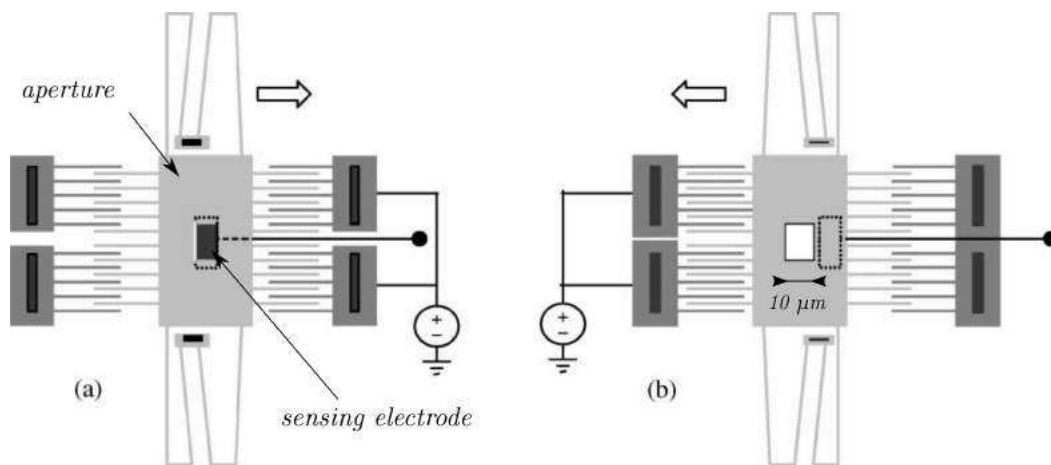


Figure 2.8.: Working principle of a MEMS field mill.

With this technology a structure can be fabricated that acts like its macroscopic counterpart. In Fig. 2.8 one such device and its functionality can be seen [19]. In Fig. 2.8a the aperture exposes the sensing electrode, while in Fig. 2.8b it shields the

electrode from the field, therefore acting like a field mill with transversal movement instead of the rotational movement of a conventional mill.

Further approaches include vertically moving shutters [20], micro-spring supported membranes [21] and similar.

## 2.4.2. Induction probes

This measurement principle is based upon the charging properties of electrically conducting elements [22]. One such element is put into an alternating electric field and acts as a capacitor with the ground as the second electrode (Fig. 2.9).

Instead of moving one of the electrodes as the before mentioned methods did, the induction probe is held steady inside of the electric field. The charges are induced when the electric field is changing its direction, hence it is only viable to use in an alternating field. Due to the induced charges the capacitive load of the sensor is changing which allows to obtain the electric field via Eq. (2.36).

The measured current can be written as:

$$i(t) = K \omega \varepsilon_0 E \cos(\omega t), \quad (2.36)$$

with  $K$  as a factor considering the electrode material and  $\omega$  the frequency of the electric field.

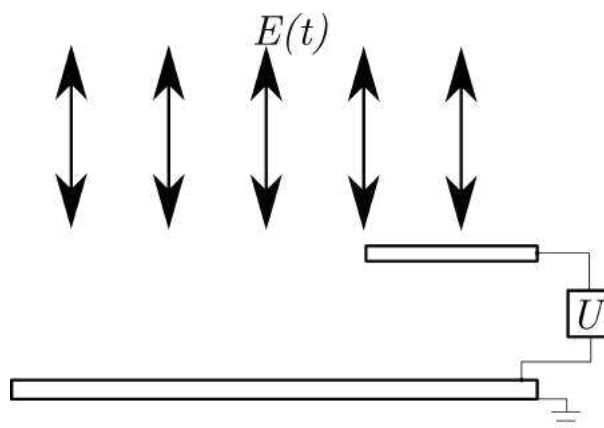


Figure 2.9.: Principle of an induction probe

### 2.4.3. Optical sensors

Optical measurement of electric fields can be accomplished by using materials which change their refractive index based upon the electric field [23]. Via the external electric field, the movement of the electrons inside the electro-optical material is restricted to the direction of said field, changing the refractive properties of the material accordingly. The refractive index  $n$  can be described via the series

$$n(E) = n_0 + S_1E + S_2E^2 + \dots, \quad (2.37)$$

with  $E$  as the electric field,  $n_0$  as the refraction index at  $E = 0$  and  $S_i$  as coefficients. The linear part of the equation is described by the Pockels-effect [24], where modulation of the refractive index  $\Delta n$  can be calculated via

$$\Delta n = n_0^3 r_{\text{eff}} \mathbf{E}. \quad (2.38)$$

$r_{\text{eff}}$  being the electro-optical tensor describing the orientation of the crystal and the polarisation of the light. The quadratic part of Eq. (2.37) is described by the Kerr effect [25], which can be expressed by

$$\Delta n = \lambda K \mathbf{E}_K^2. \quad (2.39)$$

Here  $\lambda$  describes the wavelength and  $K$  is a constant. For measurement purposes a linear effect has obvious advantages but it has to be taken into account that the sensor will be subjected to a significant drift.

The main advantage of these sensors is that they do not influence the external field because of their non-conducting properties. The downside is their inability to measure DC fields.

## 3. Sensor Design

The sensor was designed with the goal of a high field resolution. Therefore it was most suitable to use MEMS technology. To achieve cantilever dimensions of  $5\ \mu\text{m} \times 100\ \mu\text{m} \times 1000\ \mu\text{m}$  while maintaining the needed conductivity, highly doped silicon was used.

Beforehand, the different cantilever structures were simulated with the COMSOL-Multiphysics software to make sure that the resonances of the different sensors are in the right frequency range and check for potential issues.

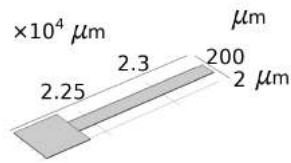
The manufacturing required an accurate design beforehand which was achieved by a Python tool during this thesis.

There were three different main shapes resembling the structure of the letters I, U and T, hence their respective names I-,U-,T-cantilever are used subsequently. The U- as well as the T-cantilevers were divided further into cantilevers with and without combs. These combs were applied to increase the capacity of the configuration and, hence, the charge.

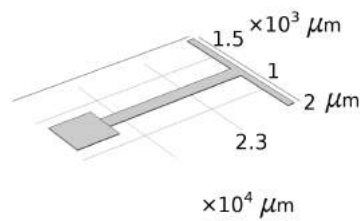
### 3.1. Mask Design

The design of the wafer mask was done with a high variability of the sensor attributes in mind. The behavior of the cantilever sensor in an electric field is mainly given by its responsivity, which is determined by the capacity of the cantilever in relation to the surrounding ground and its mechanical eigenfrequency.

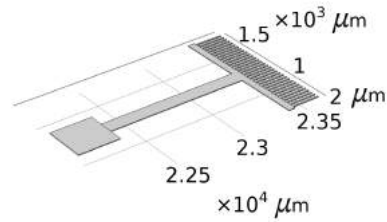
The first version and most basic type of sensor was a simple I-cantilever as seen in Fig. 3.1a. The second type was a T-cantilever with a higher capacitive area and a lower eigenfrequency because of the added mass at the end of the beam as seen in Fig. 3.1b. The third structure had added combs at the cross-beam influencing mainly the capacity as seen in Fig. 3.1c. The fourth version of cantilever was a



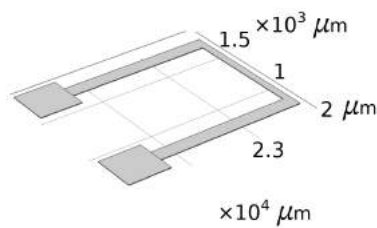
(a) I-cantilever.



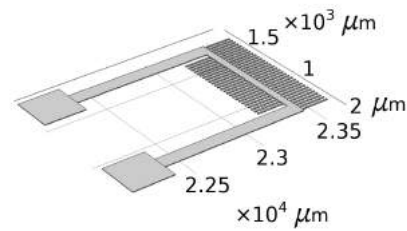
(b) T-cantilever without combs.



(c) T-cantilever with combs.



(d) U-cantilever without combs.



(e) U-cantilever with combs.

Figure 3.1.: The five different cantilever types which were simulated.

U-shaped one changing the capacity as well as the eigenfrequency via the added mass at the end of the beam and the second parallel beam as seen in Fig. 3.1d. The fifth and last structure was a U-shaped beam with added combs as seen in Fig. 3.1e.

One wafer with a diameter of 100 mm can contain 146 individual chips with a size of  $6 \times 6 \text{ mm}^2$ . An individual chip holds up to four I-cantilevers or up to two T-/U-cantilevers. Since the handling of those chips is very delicate and to investigate reproducibility, two chips of each I-structure and four chips of each T-/U-structure were produced. Their layout was drawn with a Python script, written in the scope

of this thesis.

One of the main requirements was that the script is easy to use with as few input parameters as possible but as many as necessary. In the final version, the general shape of the cantilever (I,T,U), the length and width of the beam, the length and width of the cross beam and the existence of combs was adjustable.

In total 6 chips of I-cantilevers with 3 different lengths have been produced. Furthermore, 64 chips of T-/U-cantilevers with 3 lengths, 3 cross-beam lengths and 2 comb-setups (combs / no combs) were manufactured. Additionally, 10 chips were fabricated with U-cantilevers where one of the sensors was working as a electric field sensor and the other was coated with a conducting layer, facilitating the sensing of magnetic fields. In total 38 different layouts were processed.

## 3.2. Simulation

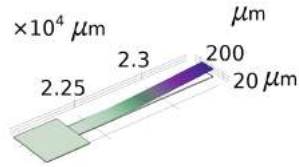
To check the eigenfrequencies as well as potential issues the structures had to be simulated beforehand. As stated above, the simulation of the cantilevers was done in COMSOL Multiphysics.

All 38 layouts were taken into account and subsequently investigated. The outcome of a selected few of these simulations can be seen in Fig. 3.2.

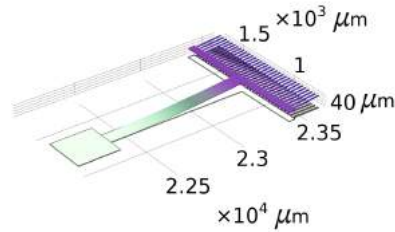
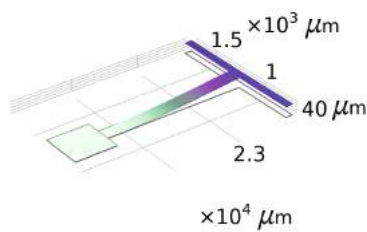
In Tab. 3.1 the numerical eigenvalues of the simulated I-shaped beams are listed, while the results of the T- and U- shaped ones listed in the Appendix A.1. The conclusion of these results was that the eigenmodes resulting in a bending oscillation, especially the second mode, are not as defined as hoped, with them not being as far apart from torsional eigenmodes.

<b>I-cantilever (width = 100 <math>\mu\text{m}</math>, height = 5 <math>\mu\text{m}</math>)</b>		
length ( $\mu\text{m}$ )	simulated eigenfrequency first mode (Hz)	simulated eigenfrequency second mode (Hz)
1000	6917	—
2000	1725	34328
3000	758	15289

Table 3.1.: Eigenfrequencies of the different I-cantilever varieties.

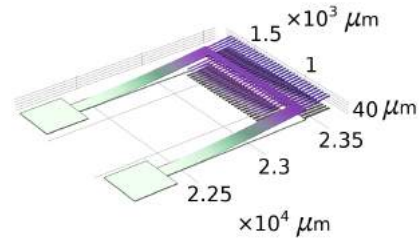
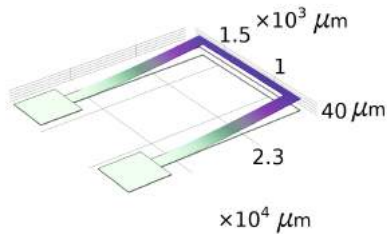


(a) Simulated I-cantilever at the first eigenmode.



(b) Simulated T-cantilever without combs at the first eigenmode.

(c) Simulated T-cantilever with combs at the first eigenmode.



(d) Simulated U-cantilever without combs at the first eigenmode.

(e) Simulated U-cantilever with combs at the first eigenmode.

Figure 3.2.: Results of the simulation of the five different types of cantilever.



### 3.3. Manufacturing

The manufacturing process of the MEMS cantilever chips requires several steps [9]. As base an SOI wafer (silicon on insulator) with a diameter of 100 mm and a specific resistance of the device layer of less than  $0.01 \Omega\text{cm}$  was used. The handle-layer with a thickness of  $350 \mu\text{m}$  ensured mechanical stability of the chip. On top of this handle-layer, a  $\text{SiO}_2$  layer is placed serving as an insulator. The device-layer on top of the  $\text{SiO}_2$  contains the actual cantilever structures. As the last layer a conductive Cr/Au-coat serves as bondpads, acting as the contact point for the applied potential.

In the following, the fabrication of the individual sensor-chips is described, as seen in Fig. 3.3. Starting with the  $\text{Ø}100$  mm-wafer the device layer had to be processed. By using the method of photolithography the pattern of the bondpads was applied and subsequently the Cr/Au layers were deposited by physical vapor deposition. Afterwards the remaining photoresist was removed. The pattern of the cantilever structures was applied, once again by a photolithographic process. The wafer then was processed further by deep reactive ion etching (DRIE, Bosch process). After this step the device layer was coated with photoresist once more to protect the cantilevers during further processing.

The last step providing a working sensor is the backside etching. To ensure that the cantilever is able to move freely, the handle layer had to be removed on the backside of the structures. Again, the backside excluding the area beneath the cantilever was coated with photoresist and treated with DRIE, therefore removing the handle layer underneath the cantilever. The last remaining layer which had to be treated was the  $\text{SiO}_2$ -layer in order to release the cantilevers. It was processed with BHF, etching the insulating layer. Afterwards, the wafer was diced into individual chips with a wafer saw. As the last step the photoresist was removed from the top side of the single chips.

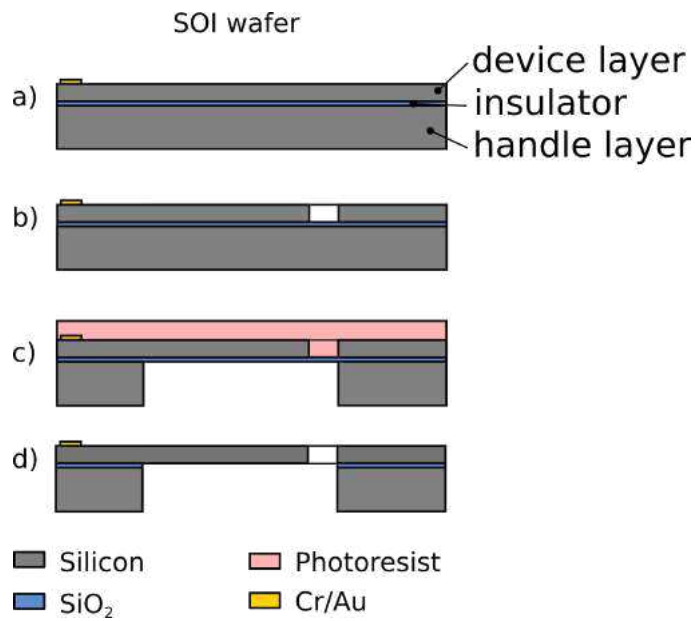


Figure 3.3.: Fabrication process of the MEMS devices.

- a) Photolithographic processing of the conductive layer.
- b) DRIE of the cantilever structure. c) Photoresistive Coating.
- d) Backside etching to release the cantilever structure.

The process described above yielded 24 I-, 24 T- as well as 22 U-cantilevers. Because of their physical dimensions the structures are rather delicate to handle which lead to the fact that not all of them could be processed to the stage in which they could be measured. Some were damaged during fabrication and handling.

## 4. Measurements

The focus of this thesis was to measure and characterize as many diverse forms of cantilever-sensors as possible to find the best combination of mechanical and electrostatic properties. For this purpose we used 6 chips of I-, 12 chips of T- and 11 chips of U-cantilevers.

In the following the setup used to generate the electric field as well as the driving mechanism of the sensors and the response measurement are described in Sec. 4.1 and the measurement itself in Sec. 4.2.

### 4.1. Measurement setup

The measurement setup can be divided into 4 parts, the field generator providing the electric field, the signal generator supplying the sensor with its driving frequency, the sensor itself and the readout measuring the response of the sensor to the field. The main setup is depicted in Fig. 4.1.

#### 4.1.1. Field generation

One of the most important factors to produce reliable data is concerning the generation of the measured electric field. To achieve a field as uniform as possible, two parallel plates with dimensions of 10 cm  $\times$  10 cm (greatly exceeding the sensor dimensions) and a distance of 1cm with a narrow hole ( $\varnothing$ 3mm) for the laser of the laser-Doppler vibrometer were used (Fig. 4.2).

As a voltage supply for the field plates two different possibilities were used, for one the Leader LPS-152. It is capable of both an output of 0 V to 25 V at 0 A to 1 A with a low voltage-resolution or an output of 0 V to 6 V at 0 A to 5 A with high voltage-resolution. The output of this voltage supply was amplified by the Tabor

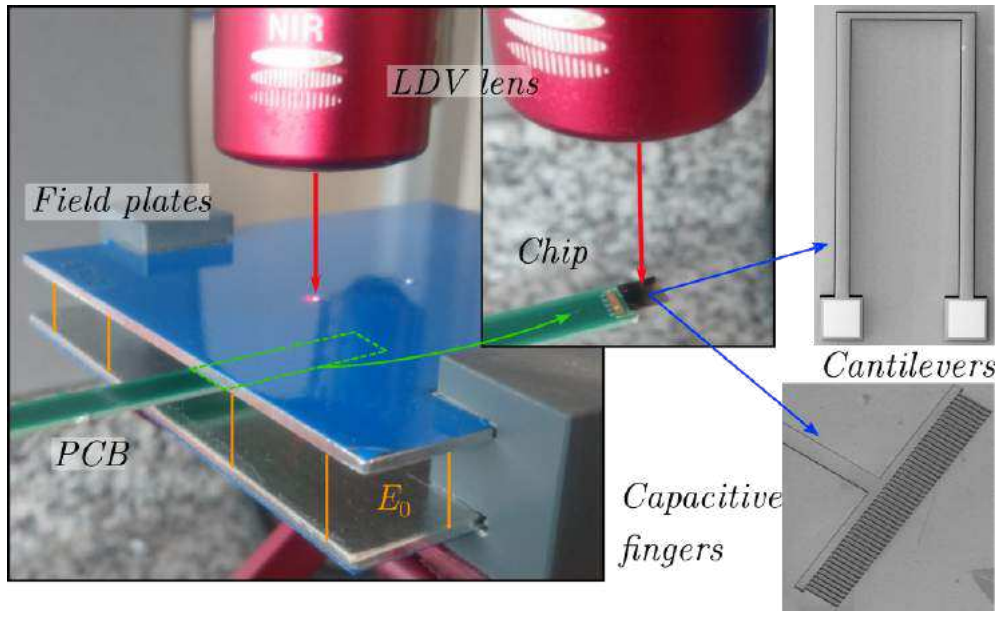


Figure 4.1.: Measurement Setup.

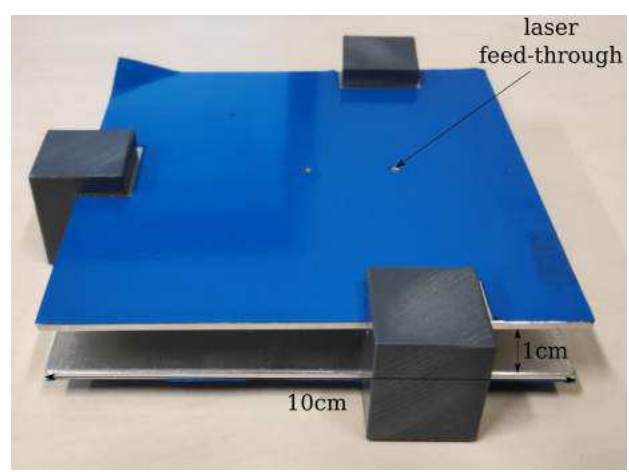


Figure 4.2.: Field generating plates.

Electronics wideband amplifier 9200A by a factor of 50 with a maximum output of 200V. Therefore, fields of up to 200V/cm or 20kV/m were available.

One important factor of this power supply is the ground connection. By using the before mentioned voltage supply - amplifier combination one field plate is automatically grounded via the amplifier. That led to the use of the second power supply, the Delta Elektronika SM 3004-D. This supply does not need to be connected to an amplifier to achieve an output voltage of 200 V and therefore the ground-connection is optional. Its operating range is given from 0 V to 300 V at 0 A to 2 A. The ground connection proved problematic during the measurement because of the ground connection of the sensor. A coupling of them over the ground is cause of a field distortion subsequently altering the measurement.

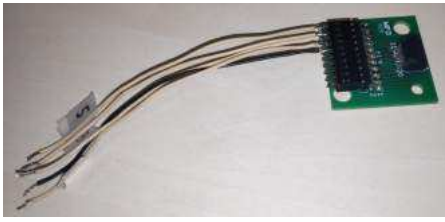
Both power supply alternatives have been used and they proved to be mostly equivalent. As stated above the Delta supply provided the option of removing the ground connection and was therefore used more frequently, although mostly grounded. Measurements with floating potential (without ground connection) are subject to further research.

#### 4.1.2. Sensor Control

To achieve the highest possible flexibility, while maintaining a sufficient accuracy, a frequency generator (Agilent 33220A Waveform Generator) was used. This device is capable of producing an output waveform with a frequency from 1  $\mu$ Hz to 20 MHz at a resolution of 1  $\mu$ Hz and an accuracy of  $\pm (10 \text{ ppm} + 3 \text{ pHz})$ . The amplitude of the signal can be modulated from 10mV<sub>pp</sub> to 10V<sub>pp</sub> (V<sub>pp</sub>...peak to peak voltage) and a DC-offset of  $\pm 5 \text{ V}$ .

This generator was used to drive the sensor structures at their respective eigen-frequencies, ranging from 100 Hz to 50 kHz at a peak-to-peak voltage of 2 V. The signal was simultaneously displayed at an oscilloscope.

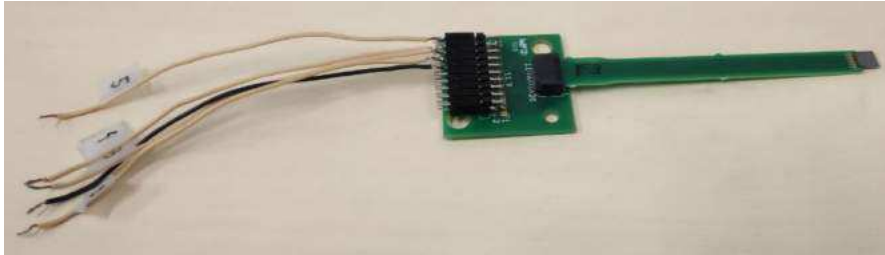
This waveform generator was controlled with a Python script in order to automate the measurement procedure.



(a) Mount for the PCB chip carrier ensuring easy interchangeability of the chips.



(b) PCB chip carrier with sensorchip bonded to its tip.



(c) The mounted sensor chip on the PCB.

Figure 4.3.: Mechanism to supply the chips with the respective signal.

### 4.1.3. Sensor

To create a convenient way of supplying the sensor with the necessary signal a mount was created. The signal provided by the waveform generator is supplied via the mount in Fig. 4.3a to the PCB chip carrier in Fig. 4.3b and, in turn, to the sensor chip bonded at its tip. The electrical connection between the chip and the carrier is one of the most sensitive joints of the whole sensor. Therefore it had to be handled with utmost caution.

The choice of material of the carrier seemed unproblematic at the beginning but turned out to be one of the major problems when measuring with this device. The material is a dielectric to minimize the influence of the sensor on the measured field. It turned out that this material is the cause of disturbances in the measured signal. More on this issue will be elaborated upon in chapter 6.2.

A schematic of the sensor inside the setup can be seen in Fig. 4.8. To supply the sensor with the needed alternating voltage, the grounded region as well as the cantilever itself are designed with designated bondpads (② & ③). The selected material of those bondpads is gold to ensure an ohmic electric contact and the ability to wire bond the chips.

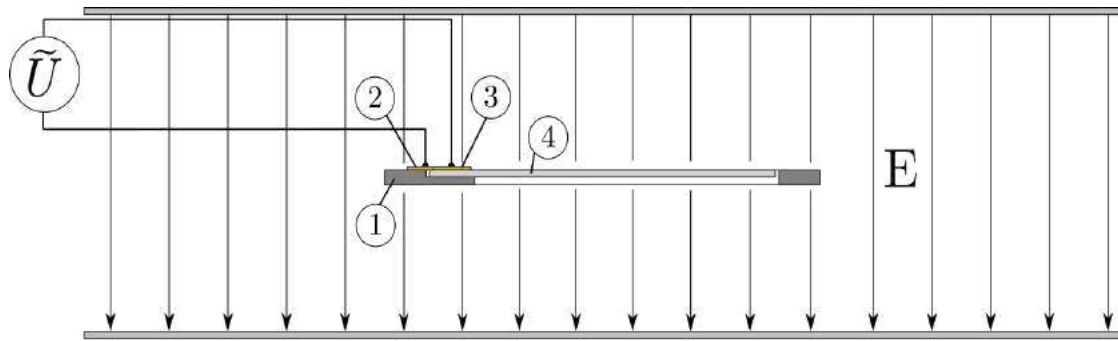


Figure 4.4.: Schematic of a lock-in amplifier.

- E...electric field,  $\tilde{U}$ ...alternating excitation,  
 ① Ground, ② Bondpad ground, ③ Bondpad cantilever,  
 ④ Cantilever, ⑤ Field plates.

#### 4.1.4. Readout

The measurement setup in the laboratory consisted of a laser-Doppler vibrometer and a lock-in amplifier.

**Laser-Doppler vibrometer** The laser-Doppler-vibrometer is a device which is capable of measuring the velocity of a sample with a high resolution. In Fig. 4.5, a schematic of the vibrometer is depicted. The laser beam with frequency  $f_0$  is divided into a reference beam and a sample beam by a beam splitter. The reference beam is reflected into another beam splitter, while the sample beam is sent through a Bragg-cell to shift its frequency into a range, which can be handled more conveniently. When hitting the target the beams frequency is Doppler-shifted to

$$f_d = 2 \frac{v}{c} (f_0 + f_b), \quad (4.1)$$

with  $f_d$  as the shifted frequency and  $f_b$  as the frequency shift due to the Bragg cell.

The sample beam and the reference beam interfere with each other resulting in a beat frequency. The intensity of this frequency is then measured by the detector.

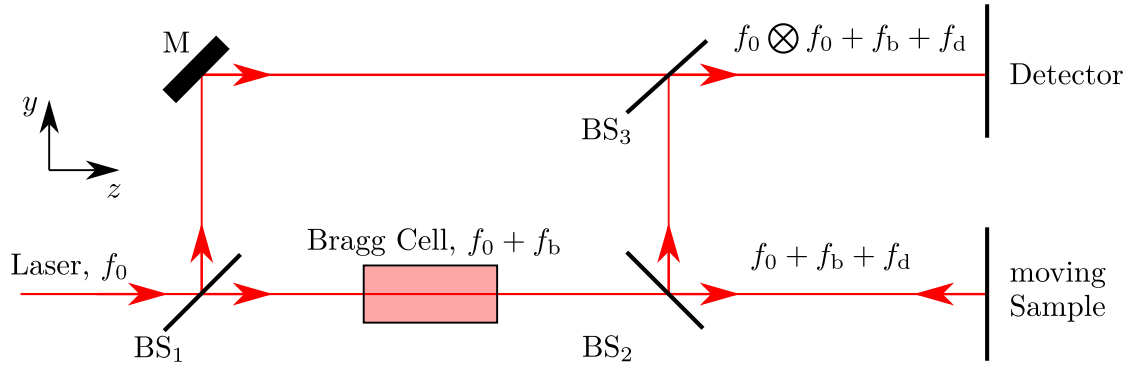


Figure 4.5.: Principle of the laser-Doppler-vibrometer. The laser beam  $f_0$  is split into two separate beams via a beam splitter ( $BS_1$ ), the reference and sample beam. The sample beam is sent through a Bragg cell and another beam splitter ( $BS_2$ ) onto the sample, where it is reflected and sent back through the beam splitter ( $BS_2$ ) into another beam splitter ( $BS_3$ ). The reference beam is reflected into the beam splitter ( $BS_3$ ) as well, where it is superimposed with the sample beam. The detector then measures the interference, concluding the movement of the sample.

The beat frequency of the two laser beams can be detected via an added Fourier component in the resulting signal. To measure this component, a linear detector is not sufficient. Since the response of photodetectors is proportional to the square of the incident radiation electric field, they are the method of choice.

The detected signal and its SNR (signal-to-noise ratio) can be calculated as follows.

The intensity of a specific electric field of the interfering beam is given as

$$I = c \varepsilon_0 E^2, \tag{4.2}$$

$$E = E_{\text{sample}} \cos(\omega_{\text{sample}} t) + E_{\text{ref}} \cos(\omega_{\text{ref}} t), \tag{4.3}$$

with  $\omega$  as the angular frequency. When taking into account that the detector



averages over short time periods, this results in an overall intensity of

$$I = c\varepsilon_0 \left( \frac{1}{2} E_{\text{sample}}^2 + \frac{1}{2} E_{\text{sample}}^2 \cos(2\omega_{\text{sample}} t) + \frac{1}{2} E_{\text{ref}}^2 + \frac{1}{2} E_{\text{ref}}^2 \cos(2\omega_{\text{ref}} t) \right. \\ \left. + E_{\text{sample}} E_{\text{ref}} (\cos((\omega_{\text{sample}} - \omega_{\text{ref}}) t) + \cos((\omega_{\text{sample}} + \omega_{\text{ref}}) t)) \right) \quad (4.4)$$

One interesting feature of the laser-Doppler vibrometer is that the noise can be reduced to the shot noise by increasing the intensity. The shot noise is the only kind of noise scaling with the squareroot of the intensity. To calculate the SNR, the intensity is separated into its AC and DC components,  $I = I_{\text{AC}} + I_{\text{DC}}$ .

$$I_{\text{DC}} = \frac{c\varepsilon_0}{2} (E_{\text{sample}}^2 + E_{\text{ref}}^2). \quad (4.5)$$

$$I_{\text{AC}} = 2 \frac{E_{\text{sample}}^2 E_{\text{ref}}^2}{E_{\text{sample}}^2 + E_{\text{ref}}^2} I_{\text{DC}} \quad (4.6)$$

For  $\frac{E_{\text{sample}}}{E_{\text{ref}}} \ll 1$ ,  $I_{\text{AC}}$  can be simplified to

$$I_{\text{AC}}^2 = 2 \left( \frac{E_{\text{sample}}}{E_{\text{ref}}} \right)^2 I_{\text{DC}}^2 = 2 \frac{P_{\text{sample}}}{P_{\text{ref}}} I_{\text{DC}}^2. \quad (4.7)$$

with  $P$  as the power of the beam.  $I_{\text{DC}}$  can be written as

$$I_{\text{DC}} = \frac{\eta e P_{\text{ref}}}{h \nu}, \quad (4.8)$$

with  $\eta$  denoting the quantum efficiency of the detector,  $e$  as an electron charge,  $h$  as the Planck constant and  $\nu$  as the frequency of a photon.

The shot noise scales with the intensity as follows

$$\overline{I_{\text{N}}^2} = 2 e I_{\text{DC}} \Delta f, \quad (4.9)$$

where  $\Delta f$  is the bandwidth of the detector's band-pass filter.

Summarized, the SNR can be written as

$$SNR = \frac{\overline{I_{\text{AC}}^2}}{\overline{I_{\text{N}}^2}} = \frac{\eta P_{\text{sample}}}{h \nu \Delta f} = \frac{\eta (\text{photons per second})}{\Delta f}. \quad (4.10)$$

**Lock-in amplifier** This measurement method was further improved by the use of a lock-in amplifier. The one at hand was the Stanford Research Systems model SR830. A basic lock-in amplifier is capable of improving the measured signal quality by eliminating all but one frequencies.

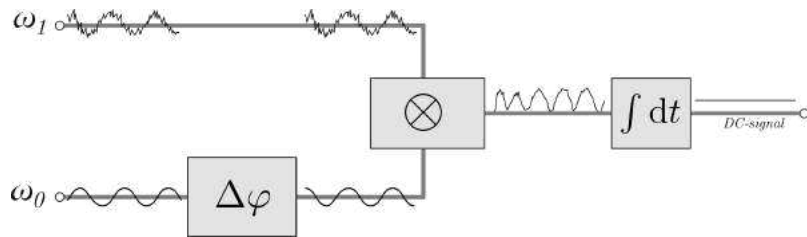


Figure 4.6.: Schematic of a lock-in amplifier.

$\omega_0$ ...reference signal,  $\omega_1$ ...measurement signal,  
 $\Delta\varphi$ ...phase shifter,  $\otimes$ ...signal multiplier,  
 $\int dt$ ...low-pass filter.

As seen in Fig. 4.6 the measurement signal is multiplied by a reference signal which itself is phase aligned to the measured signal. The result is sent into a low-pass filter (integrator) which yields the amplitude of the original frequency. To improve the signal as much as possible the phase shift between the measured signal and the reference should be as low as possible, ideally zero. This requirement is taken care of by the phase shifter.

The product of the input signal  $U_1 = V_1 \sin(\omega_1 t + \Theta_1)$ , with  $V_1$  as its amplitude,  $\omega_1$  as the signal frequency and  $\Theta_1$  as the phase, and the reference signal  $U_0 = V_0 \sin(\omega_0 t + \Theta_0)$  leads to

$$V_{\text{out}} = \frac{1}{2} V_1 V_0 \cos([\omega_0 - \omega_1]t + \Theta_1 - \Theta_0) - \quad (4.11)$$

$$\frac{1}{2} V_1 V_0 \cos([\omega_0 + \omega_1]t + \Theta_1 + \Theta_0) \quad (4.12)$$

The lowpass filter eliminates all frequencies except  $\omega_1 = \omega_0$ , yielding a voltage of

$$V_{\text{out}} = \frac{1}{2} V_1 V_0 \cos(\Theta_1 - \Theta_0), \quad (4.13)$$

which is a DC signal proportional to the amplitude of the original signal.

One more advanced approach would be the two-phase lock-in amplifier. It takes advantage of the fact that a sine with a phase shift of  $90^\circ$  becomes a cosine by utilizing two detectors. The output of the original signal ( $X$ ) and the modulated one ( $Y$ ) approximately will be

$$X \approx V_1 \cos(\Theta) \quad (4.14)$$

$$Y \approx V_1 \sin(\Theta) \quad (4.15)$$

$$\text{with } \Theta = \Theta_1 - \Theta_0 \quad (4.16)$$

The signal of both of them leads to a signal vector  $R$  with a phase  $\theta$

$$R = \sqrt{X^2 + Y^2} \quad (4.17)$$

$$\theta = \arctan\left(\frac{Y}{X}\right). \quad (4.18)$$

The main advantage of this method is the phase independent measurement of the amplitude  $R$ , while the phase is still derivable.

## 4.2. Measurements

To characterize the different manufactured structures of electric field sensors a reliable and accurate way of driving them as well as reading their signal had to be utilized. The driving mechanism provides the needed reliability and an accuracy down into the  $\mu\text{Hz}$  range. The used readout is a well-known instrument, used over many research topics and capable of providing the needed accuracy when combined with the used lock-in amplifier.

This equipment as well as a script written in Python enabled an automated characterisation and measurement of the cantilever structures as accurately as possible. The electric field used as reference was provided by the field plates described in Sec. 4.1.1. This lead to an electric field of  $E = 200 \text{ V/cm}$  for all further measurements.

The cantilevers were supplied with an alternating voltage at their respective eigen-

frequency by the waveform generator described in Sec. 4.1.2. The amplitude and the frequency of this input signal were both controlled by the measurement script. Furthermore, the signal was visualized with an oscilloscope and used as trigger for the laser-Doppler vibrometer as well as the lock-in amplifier.

The laser of the vibrometer used to acquire the velocity of the cantilever-tip was sent through the hole in the upper field plate and reflected by the cantilever. The resulting optical signal was consequently measured by the vibrometer passing on the corresponding voltage output to the lock-in amplifier where it was further provided to the script to be processed.

Two types of measurements were performed. First, a frequency sweep for identifying the oscillation modes and the quality factor and second, an amplitude sweep to obtain the responsivity. The frequency sweep, as its name implies, varies the frequency at several given peak-to-peak voltages. The specific voltage values were chosen differently from chip to chip but they all ranged from 0.1 V to 2 V and included 1 V. The second measurement conducted, the amplitude response, covered the change in signal when the amplitude of the alternating voltage, the cantilevers were supplied by, was altered at a given frequency. The amplitude was changed in logarithmic steps from 0.02 V to 2 V.

With the theoretical background in mind, the I-shaped cantilevers were expected to yield the best fitting results. With respect to the other shapes these were the easiest to manufacture, having the smallest margin of error because of their rather simple geometry. The I-cantilevers also differed in only one parameter, the length. Another advantage of this shape was their space requirement. In contrast to the other types four such cantilevers could be placed on one chip and therefore were characterized during one measurement cycle.

When considering the capacity between the cantilever and the surrounding ground as being constant, which is viable for small deflection  $w \ll h$ , the movement and total deflection of the sensor could be calculated by only taking mechanical effects and the force of the sensor due to the electric field into account. According to the mechanical theory their deflection should change with their length to the power of

three, as

$$\begin{aligned}w(x) &= \frac{qx^2}{24E_y I_y} (6L^2 - 4Lx + x^2) \\ \Rightarrow w(L) &= \frac{FL^3}{8E_y I_y} \text{ with } q = \frac{F}{L} \\ \Rightarrow F &= \frac{8wE_y I_y}{L^3},\end{aligned}\tag{4.19}$$

while the electrostatic force between the field and the cantilever should change linearly over the length of the sensor.

The second shape we looked at were the T-cantilevers. Because of the width of the cross beam only two of them could be placed on one chip. They were expected to have a lower eigenfrequency because of the added mass at the tip of the beam due to the cross beam. Another interesting fact about the T-shaped cantilevers is the added capacity, which was expected to yield a higher deflecting force. This was expected to be the dominating factor especially for the beams with added combs, due to the bigger capacitive length.

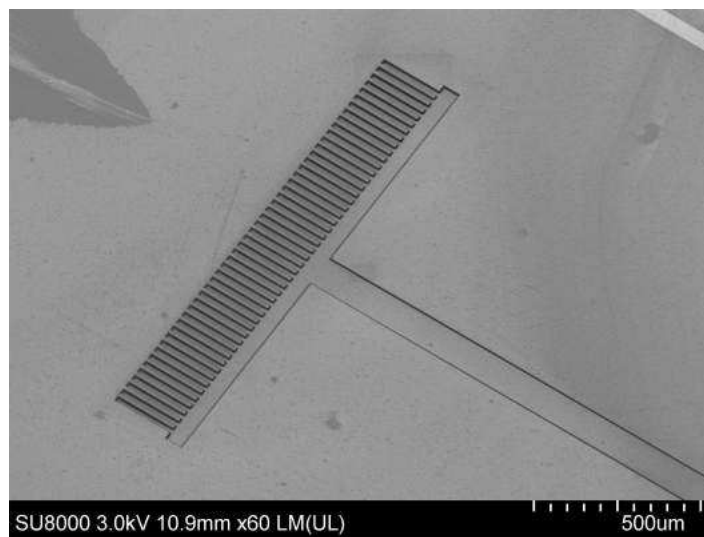


Figure 4.7.: SEM-picture of the T-shaped cantilever.

Particular attention had to be placed upon the ones with added combs. Those combs had a rather delicate structure because of their geometric measurements.

The last measured shape were the U-beams. They were expected to behave as complex as the T-shapes but with an added beam and therefore an additional mechanical stiffness. Ultimately they were approximated as a beam with double the width and the added cross beam. This form of sensor had the added difficulty of torsional oscillation modes which may have been able to interfere with the measurements. One significant benefit of those cantilevers was the capability of providing a closed conducting path yielding the possibility of acting as a magnetic field sensor when a current is transmitted.

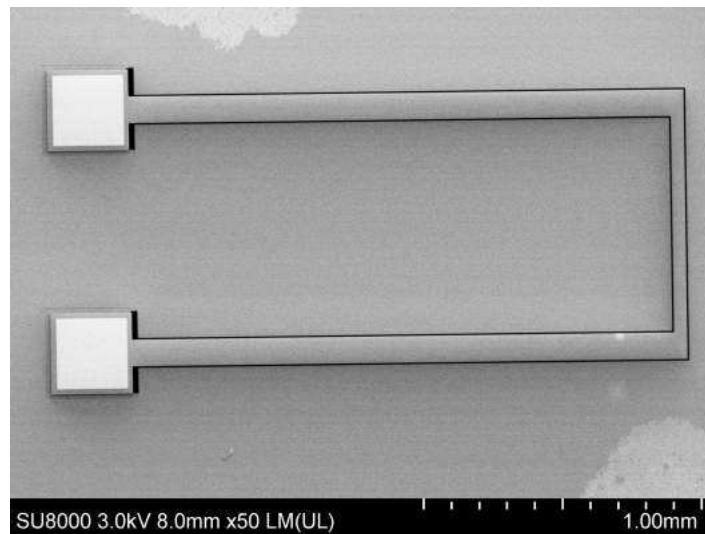


Figure 4.8.: SEM-picture of the U-shaped cantilever.

By adding a layer of gold by vapor deposition on top of one cantilever and keeping the other as is, the possibility of a sensor measuring electric as well as magnetic fields arose. Depending on which sensor is driven the measured physical quantity could be changed from electric field to magnetic field and vice versa or even simultaneously if the cross talk turns out to be low enough.

On one chip a U-cantilever without the gold layer would work as the electric field sensor in the usual way, while a second one, with added gold, would be connected to a power supply. The current and therefore the moving charges would be subjected to the Lorentz force and therefore deflecting the second cantilever according to the magnetic field strength.

## 5. Results

After evaluating the results for the measured cantilever structures, the conclusion was that the change in capacity during the movement of the sensor is not as negligible as assumed. Furthermore the influence of the comb structures is clearly visible but not as prevalent as expected especially for higher cross beam lengths and therefore more fingers.

### 5.1. I-Cantilevers

The frequency sweep measurements yielded a Bode diagram. In the following, the measurement of one cantilever with a length of 3 mm is described. As visible in Fig. 5.1 the signal of the sensor depends on the excitation frequency as well as on the peak-to-peak voltage. At low frequencies ( $<200$  Hz) the signal is subject to a high noise level because of the measurement method. The laser-Doppler vibrometer measures the velocity of the cantilever, which decreases at lower frequencies. The signal to noise ratio improves at higher values and shows a constant deflection as expected in a damped driven harmonic oscillator. It then increases till it reaches the first eigenfrequency and drops afterwards again by a factor of  $1/\omega^2$ . As soon as the second eigenfrequency is approached, the signal increases again. As expected the amplitude is at its global maximum when the structure is excited at its first eigenfrequency.

In Fig. 5.1 the response function has been fitted with the ideal equation of motion for a damped driven harmonic oscillator. This allowed the extraction of the acceleration combined with the mass and therefore the force acting upon it. Furthermore the damping factor and the resonance frequency could be determined,

yielding the quality factor according to Eq. (5.1).

$$D = \frac{d}{\omega_0} \text{ and } Q = \frac{1}{2D}$$

$$\Rightarrow Q = \frac{\omega_0}{2\gamma}, \quad (5.1)$$

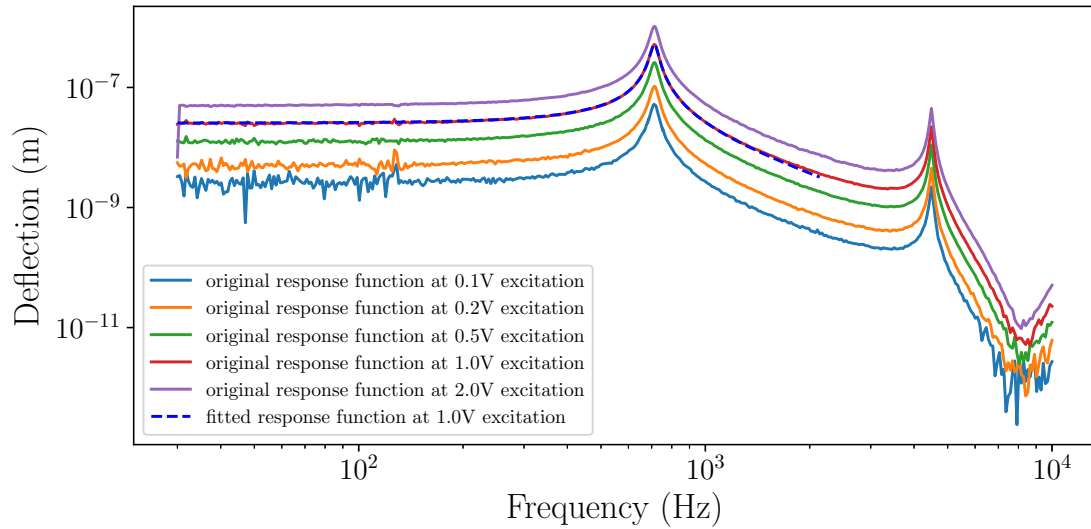


Figure 5.1.: I-cantilever. Response of an I-shaped cantilever with a length of 3 mm at different frequencies.

For the in Fig. 5.1 shown example the maximum deflection of  $1.04 \mu\text{m}$  and a quality factor of 20.5 were measured.

To compare the results of cantilevers, the respective force on it has been calculated using Eq. (4.19). To calculate the force, the deflection at eigenfrequency has been used, making it necessary to modify the deflection with the quality factor  $w_{\text{max}} = w(f = f_0) \approx Qw(f \ll f_0)$ .

$$F = \frac{8E_y I_y}{L^3} \frac{w_{\text{max}}}{Q} \quad (5.2)$$

The combined results of all I-cantilevers are shown in Fig. 5.2, in terms of the calculated force over the length. It is evident that the force acting on the cantilever increases rather linearly.



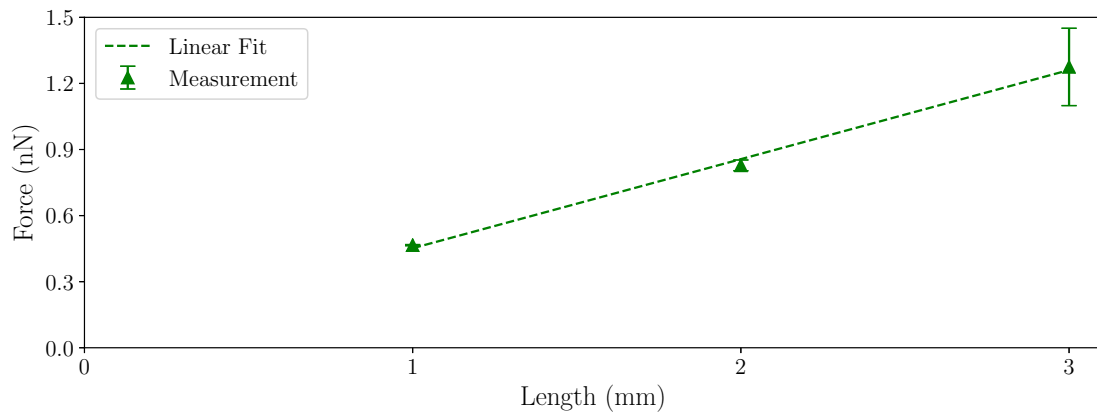


Figure 5.2.: I-cantilever. Measured force acting on the cantilever at three different lengths.

It was expected that the force is rising linearly with the length of the structure which is exactly what the measurements showed. This means that for the I-cantilevers, the assumption that the capacity is constant holds.

Another important property of this sensor type is its behavior at different voltage amplitudes. This was measured by the amplitude response measurement (Fig. 5.3).

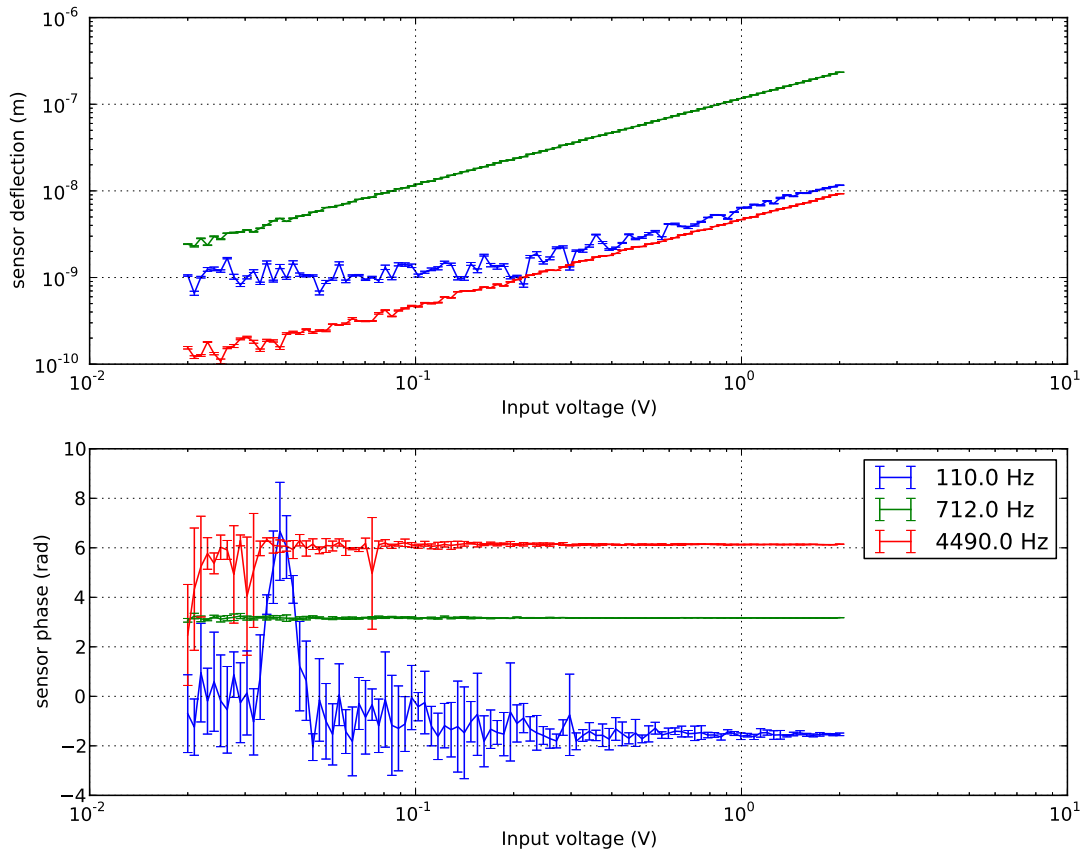


Figure 5.3.: I-cantilever. Amplitude-response of a cantilever with a length of 3mm.

The deflection of the sensor rises linearly with increased input voltage. This holds true for measurements at the eigenfrequency, which was measured to be at 712 Hz in this case. When measuring in the quasistatic regime ( $\omega \ll \omega_0$ ), here at 110 Hz, the signal becomes unstable but there is still a discernible increase in the signal.

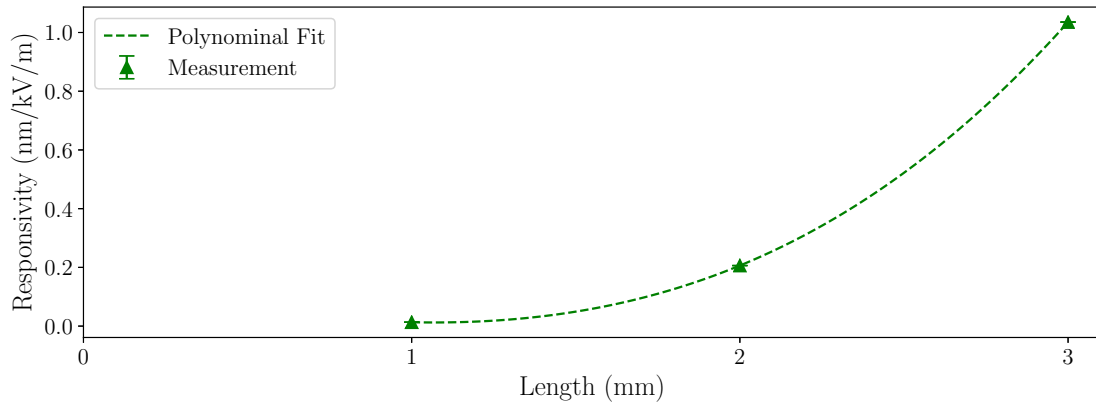


Figure 5.4.: I-cantilever. Responsivity for three different lengths.

As seen in Fig. 5.4 the responsivity of the I-shaped sensors increases steeply with the length. As calculated, the responsivity is proportional to the third power of the length. This was confirmed by the measurements.

## 5.2. T-Cantilever

The deflections of the T-shaped structures were observed to be similar to the I-shaped ones. A significant difference between them was the magnitude of the deflection. As seen in Fig. 5.5 the deflection is smaller, which is a result that requires further investigation.

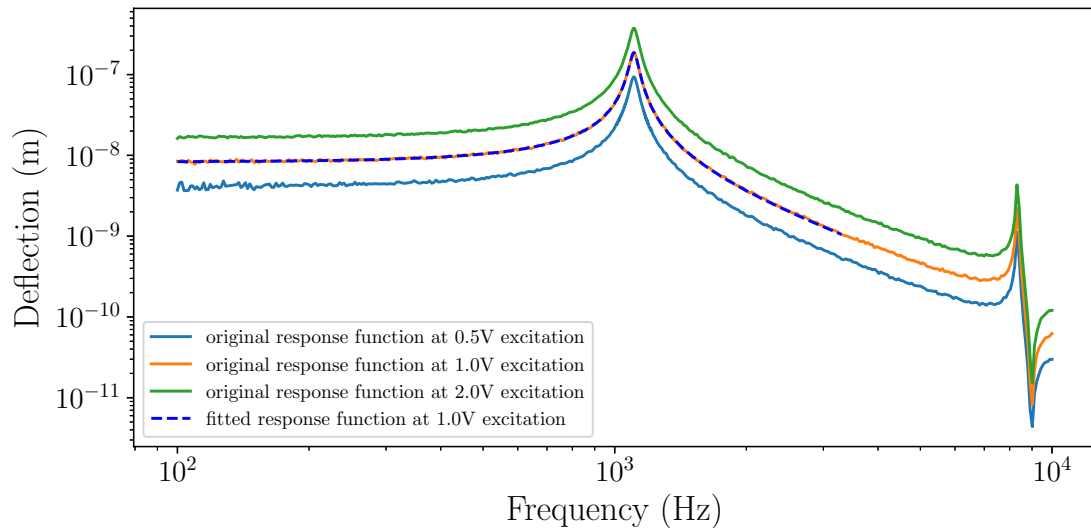


Figure 5.5.: T-cantilever without combs. Response of a T-formed cantilever with a length of 2 mm and a cross length of 1.5 mm at different frequencies.

Comparing the force response of the T-shapes with and without combs shows that the peak is wider for the ones carrying the combs (Fig.5.6). This becomes apparent when looking at the quality factor. By adding the mass of the combs, the eigenfrequency decreases and therefore the quality factor is decreased as well, broadening the peak. A more significant factor may also be the increased damping due to the added gap-length.

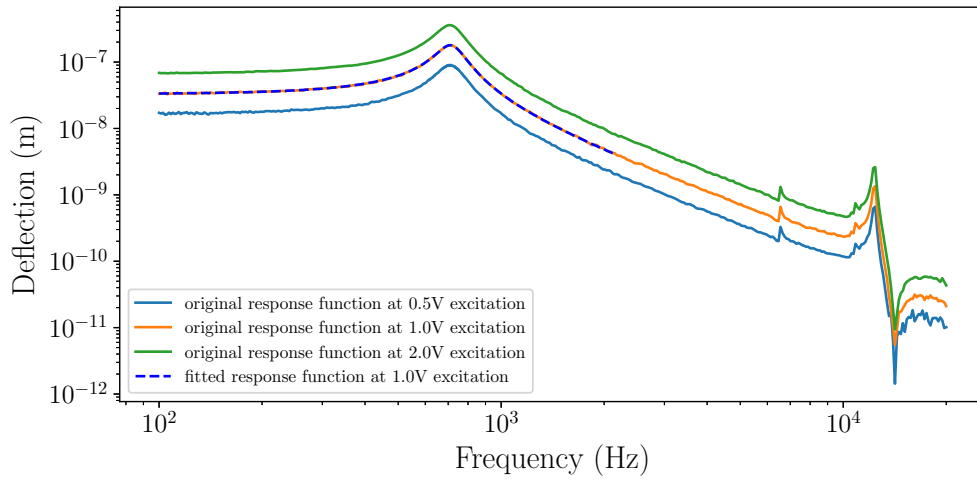


Figure 5.6.: T-cantilever with combs. Response of a T-cantilever with a length of 2 mm and a cross length of 1.5 mm at different frequencies.

When considering the response of T-shaped structures with only one cross length of 1 mm, a clear increase in force is visible over the cantilever length. In comparison to the I-cantilevers the linear behavior is replaced by a power function due to the added force at the tip (Fig. 5.8).

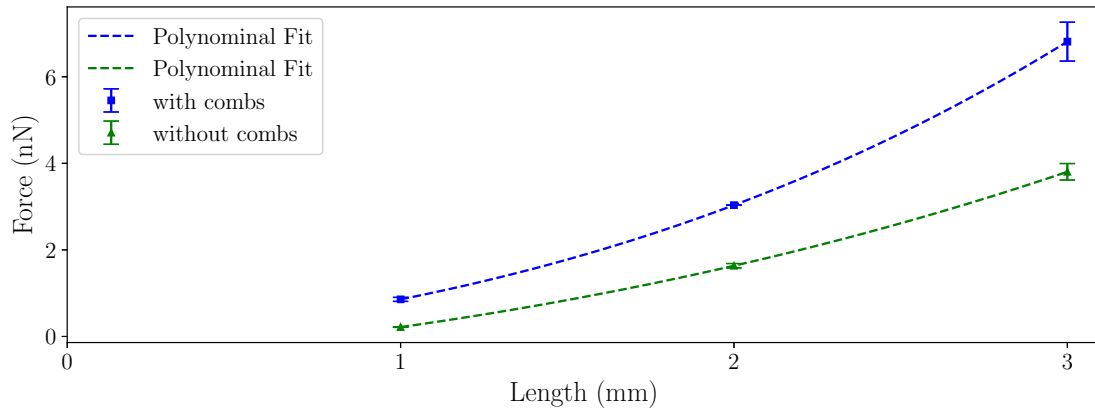


Figure 5.7.: T-cantilever. Comparison of the force acting on the cantilever at a cross length of 1 mm.

The effect of the combs over different lengths of the cross beam is depicted in Fig. 5.8. The influence of the combs is rather constant with respect to the cross length. This behavior is hard to explain and differs from the expected one. One approach may be that the cross beam experiences significant bending during the movement, but this fact will be subject to further research.

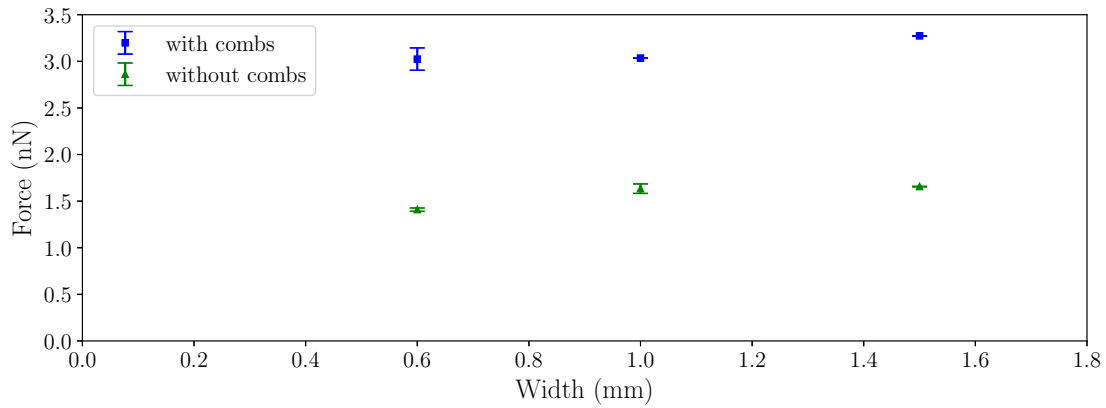


Figure 5.8.: T-cantilever. Comparison of the force acting on the cantilever at a length of 2 mm and varying cross beam widths.

### 5.3. U-Cantilever

The U-shaped sensors were expected to behave similar to the previous cantilevers. The combination of two I-shapes with a cross beam became apparent when looking at the maximum response. It was as good as the one of the I-cantilevers with the added advantage of optional comb-structures.

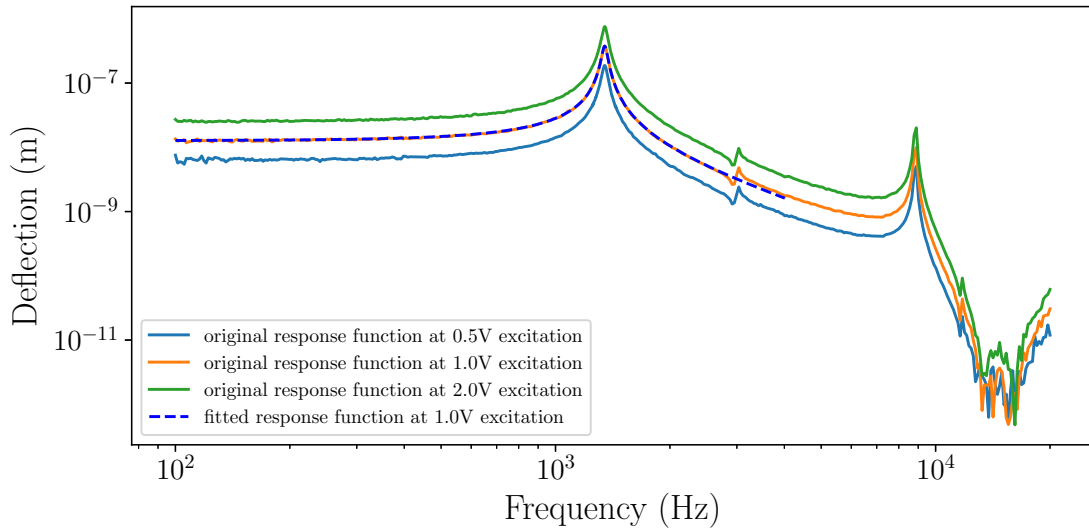


Figure 5.9.: U-cantilever without combs. Response of a U-cantilever with a length of 2 mm and a cross length of 1 mm at different actuation amplitudes.

In contrast to the other shapes, it was not possible to show a meaningful comparison between different geometries of U-cantilevers, since the ones measured were too different. As already mentioned in Sec. 4.2 a further advantage of the U-shaped sensor was their ability to be used as magnetic field sensors. With an added conduction layer on the cantilever a current was applied to one of the structures. By having two of them on one chip it is possible to measure the magnetic as well as the electric field simultaneously. However, this will be investigated within a future work.

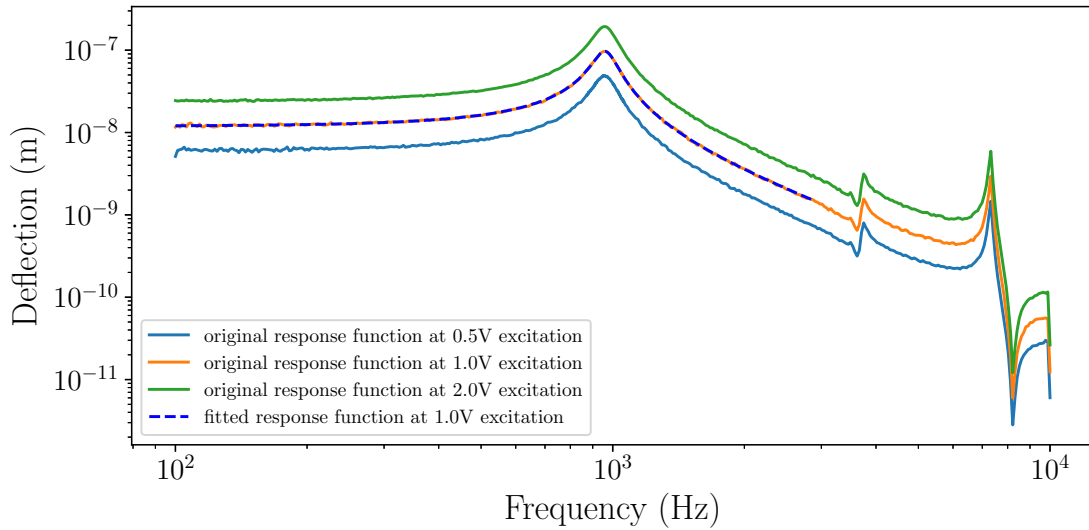


Figure 5.10.: U-cantilever with combs. Response of an U-cantilever with a length of 2 mm and a cross length of 1 mm at different actuation amplitudes.

## 5.4. PCB Carrier

During the measurements an unexpected signal was detected. First it was suspected that this signal is caused by interference of the sensor with electric fields caused by electrical equipment in the vicinity. By taking different shielding approaches the source of the signal was narrowed down to the sensor setup. During further investigation into the matter, it was concluded that the carrier for the chips, which is made from a glass-reinforced epoxy laminate material, is the reason for the strange behavior. This material should be electrically insulating, but it seems to contain charges (i.e. ions) which slowly move inside the carrier. Thus the material is slowly polarized. This leads to a changing electric field disturbing the one intended to be measured.



# 6. Conclusion and Outlook

## 6.1. Conclusion

The first part of the thesis concerned the design and manufacturing of a variety of sensor chips. The result was a script capable of automatically compiling a large number of structures by changing a small number of geometric parameters. The decisive factors of those structures included their overall shape, length, width and whether combs are to be used or not. This part showed that it was possible to fabricate such devices and utilize them as electric field sensors.

The second part, the characterization of those cantilevers issued several challenges. To prepare the sensors for the measurements they had to be bonded in order to supply the voltage. During the bonding and handling several of the structures were rendered useless. Furthermore, an appropriate mounting mechanism had to be built, which enabled the quick and easy changing of the sensors.

The characterization of the structures lead to some significant insight into their behavior under the influence of the electric field. The force experienced by the I-shaped sensors showed a rather linear behavior with varying length.

Furthermore, the effects of the combs on the force was investigated. It showed that the added combs yielded an increase in the response force, but increasing the number of combs did not impact the response force significantly, mainly due to the added cross beam length.

The most interesting shape, enabling the measurement of the electric and the magnetic field simultaneously, the U-shape, showed promising results but was also the least investigated form due to problems with the manufacturing, leading to a small number with vastly different parameters.

In summary it can be said that this method of electric field measurement is a rather promising one yielding significant advantages to the most common state-of-the-art

approaches but it is also subject to further challenges which have to be eliminated.

## 6.2. Outlook

This sensor approach looks very promising, although there is a variety of challenges to be taken on. One of those challenges regarding the control of the sensor will be to supply it with a stable and reliable signal without ground connection.

Concerning the sensor itself it will be interesting to see if a closer look into the U-shapes will yield a sensor capable of measuring magnetic and electric field. Furthermore, a closer look into the I- and T-shapes may lead to a broader and better understanding of the capacitive behavior of those sensors.

One of the most interesting phenomena observed, was a charge accumulating during the measurements of the individual cantilevers. After significant testing it has been concluded that the reason for this behavior is the slowly moving ions of the used PCB carriers. The material on which the cantilever will act on will therefore also be subject to extensive research.

The last relevant part will be the readout of the sensor. Although an interesting and working approach was already made by M. Gschirtz, MSc., there is a lot of room for improvement on this topic as well.

# A. Appendix

## A.1. Measurement results

### A.1.1. I-cantilever

<b>I-cantilever (width = 100 <math>\mu\text{m}</math>, height = 5 <math>\mu\text{m}</math>)</b>		
length ( $\mu\text{m}$ )	eigenfrequency first mode (Hz)	eigenfrequency second mode (Hz)
1000	6917	—
2000	1725	34328
3000	758	15289

Table A.1.: Eigenfrequencies of the different I-cantilever varieties.

## A.1.2. T-cantilever

T-cantilever (beam-width = 100 $\mu\text{m}$ , height = 5 $\mu\text{m}$ )			
length ( $\mu\text{m}$ )	width ( $\mu\text{m}$ )	combs	eigenfrequency first mode (Hz)
1000	1000	0	3860
		1	2549
	1500	0	3285
		1	2108
2000	600	0	1352
		1	1072
	1000	0	1202
		1	895
	1500	0	1071
		1	764
3000	600	0	642
		1	543
	1000	0	587
		1	465
	1500	0	535
		1	408

Table A.2.: Eigenfrequencies of the different T-cantilever varieties.

### A.1.3. U-cantilever

U-cantilever (beam-width = 100 $\mu\text{m}$ , height = 5 $\mu\text{m}$ )				
length ( $\mu\text{m}$ )	width ( $\mu\text{m}$ )	combs	eigenfrequency first mode (Hz)	eigenfrequency first mode (Hz)
1000	1000	0	4773	30330
		1	3105	22445
	1500	0	4182	19374
		1	2537	13191
2000	600	0	1508	9625
		1	1222	8361
	1000	0	1398	9136
		1	1032	7780
	1500	0	1289	8498
		1	886	7077
3000	600	0	695	4423
		1	598	3966
	1000	0	659	4251
		1	521	3733
	1500	0	621	4073
		1	457	3540

Table A.3.: Eigenfrequencies of the different U-cantilever varieties.

# Bibliography

- [1] Wolfgang Demtröder. *Experimentalphysik 2 (Elektrizität und Optik)*. 2013, p. 495. ISBN: 978-3-642-29943-8. DOI: 10.1007/978-3-642-29944-5. arXiv: 1011.1669. URL: <http://link.springer.com/10.1007/978-3-642-29944-5>.
- [2] *Electric field* - Wikipedia. URL: [https://en.wikipedia.org/wiki/Electric%7B%5C\\_%7Dfield](https://en.wikipedia.org/wiki/Electric%7B%5C_%7Dfield) (visited on 03/22/2020).
- [3] *Coulomb's law* - Wikipedia. URL: [https://en.wikipedia.org/wiki/Coulomb%7B%5C\\_%7D27s%7B%5C\\_%7Dlaw](https://en.wikipedia.org/wiki/Coulomb%7B%5C_%7D27s%7B%5C_%7Dlaw) (visited on 03/22/2020).
- [4] *Magnetic field* - Wikipedia. URL: [https://en.wikipedia.org/wiki/Magnetic%7B%5C\\_%7Dfield](https://en.wikipedia.org/wiki/Magnetic%7B%5C_%7Dfield) (visited on 03/22/2020).
- [5] *Lorentz force* - Wikipedia. URL: [https://en.wikipedia.org/wiki/Lorentz%7B%5C\\_%7Dforce](https://en.wikipedia.org/wiki/Lorentz%7B%5C_%7Dforce) (visited on 03/22/2020).
- [6] *Deflection (engineering)* - Wikipedia. URL: [https://en.wikipedia.org/wiki/Deflection%7B%5C\\_%7D\(engineering\)](https://en.wikipedia.org/wiki/Deflection%7B%5C_%7D(engineering)) (visited on 03/22/2020).
- [7] Silvan Schmid, Luis Guillermo Villanueva, and Michael Lee Roukes. *Fundamentals of nanomechanical resonators*. 2016, pp. 1–175. ISBN: 9783319286914. DOI: 10.1007/978-3-319-28691-4.
- [8] *Euler–Bernoulli beam theory* - Wikipedia. URL: [https://en.wikipedia.org/wiki/Euler%E2%80%93Bernoulli%7B%5C\\_%7Dbeam%7B%5C\\_%7Dtheory](https://en.wikipedia.org/wiki/Euler%E2%80%93Bernoulli%7B%5C_%7Dbeam%7B%5C_%7Dtheory) (visited on 03/22/2020).
- [9] Andreas Kainz. “Optimisation of an Optomechanical Transducer and its Application as Electric Field Sensor”. PhD thesis. TU Vienna, 2017, p. 112.
- [10] *Q factor* - Wikipedia. URL: [https://en.wikipedia.org/wiki/Q%7B%5C\\_%7Dfactor](https://en.wikipedia.org/wiki/Q%7B%5C_%7Dfactor) (visited on 03/22/2020).
- [11] Matija Kusztrich. “Design and testing of an excitation circuit for a MEMS electric field sensor”. 2020.
- [12] Martin Gschirtz. “Optical Readout for Micromechanical Electric Field Sensors”. PhD thesis. Technical University Vienna, 2020.

- [13] C. T.R. Wilson. “The electric field of a thundercloud and some of its effects”. In: *Proceedings of the Physical Society of London* 37.1 (1924). ISSN: 14787814. DOI: 10.1088/1478-7814/37/1/314.
- [14] Masaru Ishii et al. “Frequency of upward lightning from tall structures in winter in Japan”. In: *2011 7th Asia-Pacific International Conference on Lightning, APL2011*. 2011, pp. 933–936. ISBN: 9781457714665. DOI: 10.1109/APL.2011.6111049.
- [15] “WHO | Electromagnetic fields and public health”. In: *WHO* (2016).
- [16] Yong Cui et al. “Model, Design, and Testing of Field Mill Sensors for Measuring Electric Fields Under High-Voltage Direct-Current Power Lines”. In: *IEEE Transactions on Industrial Electronics* 65.1 (2018), pp. 608–615. ISSN: 02780046. DOI: 10.1109/TIE.2017.2719618.
- [17] John G. Webster. *Measurement, Instrumentation, and Sensors Handbook*. 2017, pp. 64–1–64–18. ISBN: 9781439848890. DOI: 10.1201/b15474.
- [18] H.-W. Kasemir. “Die Feldkomponentenmühle: Ein Gerät zur Messung der drei Komponenten des luftelektrischen Feldes und der Flugzeugeigenladung bei Flugzeugaufstiegen”. In: *Tellus* 3.4 (1951), pp. 240–247. ISSN: 0040-2826. DOI: 10.3402/tellusa.v3i4.8659.
- [19] Mark N. Horenstein and Patrick R. Stone. “A micro-aperture electrostatic field mill based on MEMS technology”. In: *Journal of Electrostatics* 51-52.1-4 (2001), pp. 515–521. ISSN: 03043886. DOI: 10.1016/S0304-3886(01)00048-1.
- [20] T. Chen et al. “Micromachined electric field mill employing a vertical moving shutter”. In: *Procedia Engineering* 87 (2014), pp. 452–455. ISSN: 18777058. DOI: 10.1016/j.proeng.2014.11.352. URL: <http://dx.doi.org/10.1016/j.proeng.2014.11.352>.
- [21] A. Roncin, C. Shafai, and D. R. Swatek. “Electric field sensor using electrostatic force deflection of a micro-spring supported membrane”. In: *Sensors and Actuators, A: Physical* 123-124 (2005), pp. 179–184. ISSN: 09244247. DOI: 10.1016/j.sna.2005.02.018.
- [22] R Miles et al. “Report on Non-Contact DC Electric Field Sensors”. In: (2009). URL: <https://e-reports-ext.llnl.gov/pdf/374701.pdf>.
- [23] S R M Robertson and A J Rogers. “Measurement of Dc Electric Fields Using the Electro-Optic Effect.” In: *IEE Proceedings, Part J: Optoelectronics* 132.3 (1985), pp. 195–198. ISSN: 02673932. DOI: 10.1049/ip-j.1985.0041.
- [24] *Pockels effect - Wikipedia*. URL: [https://en.wikipedia.org/wiki/Pockels%7B%5C\\_%7Deffect](https://en.wikipedia.org/wiki/Pockels%7B%5C_%7Deffect) (visited on 03/22/2020).

- [25] *Kerr effect* - *Wikipedia*. URL: [https://en.wikipedia.org/wiki/Kerr%7B%5C\\_%7Deffect](https://en.wikipedia.org/wiki/Kerr%7B%5C_%7Deffect) (visited on 03/22/2020).